



AFRL-RX-WP-TR-2010-4297

**EFFICIENT SENSITIVITY METHODS FOR
PROBABILISTIC LIFING AND ENGINE PROGNOSTICS**

Harry Millwater, Ronald Bagley, Jose Garza, D. Wagner, Andrew Bates, and Andy Voorhees
University of Texas at San Antonio

SEPTEMBER 2010
Final Report

Approved for public release; distribution unlimited.

See additional restrictions described on inside pages

STINFO COPY

**AIR FORCE RESEARCH LABORATORY
MATERIALS AND MANUFACTURING DIRECTORATE
WRIGHT-PATTERSON AIR FORCE BASE, OH 45433-7750
AIR FORCE MATERIEL COMMAND
UNITED STATES AIR FORCE**

NOTICE AND SIGNATURE PAGE

Using Government drawings, specifications, or other data included in this document for any purpose other than Government procurement does not in any way obligate the U.S. Government. The fact that the Government formulated or supplied the drawings, specifications, or other data does not license the holder or any other person or corporation; or convey any rights or permission to manufacture, use, or sell any patented invention that may relate to them.

This report was cleared for public release by the USAF 88th Air Base Wing (88 ABW) Public Affairs Office (PAO) and is available to the general public, including foreign nationals. Copies may be obtained from the Defense Technical Information Center (DTIC) (<http://www.dtic.mil>).

AFRL-RX-WP-TR-2010-4297 HAS BEEN REVIEWED AND IS APPROVED FOR PUBLICATION IN ACCORDANCE WITH THE ASSIGNED DISTRIBUTION STATEMENT.

*//Signature//

PATRICK GOLDEN, Project Engineer
Metals Branch
Metals, Ceramics & NDE Division

//Signature//

PAUL RET, Chief
Metals Branch
Metals, Ceramics & NDE Division

//Signature//

ROBERT MARSHALL, Deputy Chief
Metals, Ceramics & NDE Division
Materials & Manufacturing Directorate

This report is published in the interest of scientific and technical information exchange, and its publication does not constitute the Government's approval or disapproval of its ideas or findings.

*Disseminated copies will show “//Signature//” stamped or typed above the signature blocks.

| REPORT DOCUMENTATION PAGE | | | | | Form Approved OMB No. 0704-0188 | |
|--|-----------------------------|------------------------------|---------------------------------------|---|---|--|
| <p>The public reporting burden for this collection of information is estimated to average 1 hour per response, including the time for reviewing instructions, searching existing data sources, gathering and maintaining the data needed, and completing and reviewing the collection of information. Send comments regarding this burden estimate or any other aspect of this collection of information, including suggestions for reducing this burden, to Department of Defense, Washington Headquarters Services, Directorate for Information Operations and Reports (0704-0188), 1215 Jefferson Davis Highway, Suite 1204, Arlington, VA 22202-4302. Respondents should be aware that notwithstanding any other provision of law, no person shall be subject to any penalty for failing to comply with a collection of information if it does not display a currently valid OMB control number. PLEASE DO NOT RETURN YOUR FORM TO THE ABOVE ADDRESS.</p> | | | | | | |
| 1. REPORT DATE (DD-MM-YY) September 2010 | | 2. REPORT TYPE Final | | 3. DATES COVERED (From - To) 02 August 2007 – 30 August 2010 | | |
| 4. TITLE AND SUBTITLE EFFICIENT SENSITIVITY METHODS FOR PROBABILISTIC LIFING AND ENGINE PROGNOSTICS | | | | 5a. CONTRACT NUMBER FA8650-07-C-5060 | | |
| | | | | 5b. GRANT NUMBER | | |
| | | | | 5c. PROGRAM ELEMENT NUMBER 62102F | | |
| 6. AUTHOR(S) Harry Millwater, Ronald Bagley, Jose Garza, D. Wagner, Andrew Bates, and Andy Voorhees | | | | 5d. PROJECT NUMBER 4347 | | |
| | | | | 5e. TASK NUMBER RG | | |
| | | | | 5f. WORK UNIT NUMBER M02R3000 | | |
| 7. PERFORMING ORGANIZATION NAME(S) AND ADDRESS(ES) University of Texas at San Antonio One UTSA Circle San Antonio, TX 78249 | | | | 8. PERFORMING ORGANIZATION REPORT NUMBER | | |
| 9. SPONSORING/MONITORING AGENCY NAME(S) AND ADDRESS(ES) Air Force Research Laboratory Materials and Manufacturing Directorate Wright-Patterson Air Force Base, OH 45433-7750 Air Force Materiel Command United States Air Force | | | | 10. SPONSORING/MONITORING AGENCY ACRONYM(S) AFRL/RXLM | | |
| | | | | 11. SPONSORING/MONITORING AGENCY REPORT NUMBER(S) AFRL-RX-WP-TR-2010-4297 | | |
| 12. DISTRIBUTION/AVAILABILITY STATEMENT Approved for public release; distribution unlimited. | | | | | | |
| 13. SUPPLEMENTARY NOTES Report contains color. PAO Case Number: 88ABW 2010-4948; Clearance Date: 10 Sep 2010. | | | | | | |
| 14. ABSTRACT Probabilistic engine health management (PHM) is expected to be a go-forward approach for the USAF and other DoD agencies to enable dramatic improvements in the assessment and management of military assets. As a result, accurate and information-rich probabilistic lifing methods are essential to assess the benefits of technology insertion programs for PHM. As such, under this program three technology thrusts were investigated: a) sensitivity methods probability-of-failure estimates with respect to POD curve parameters, b) complex variable methods for sensitivity analysis, and c) probabilistic sensitivity analysis with respect to bounds of truncated distributions. | | | | | | |
| 15. SUBJECT TERMS fatigue, crack growth, probabilistic analysis, life prediction | | | | | | |
| 16. SECURITY CLASSIFICATION OF: | | | 17. LIMITATION OF ABSTRACT: SAR | 18. NUMBER OF PAGES 58 | 19a. NAME OF RESPONSIBLE PERSON (Monitor) Patrick Golden 19b. TELEPHONE NUMBER (Include Area Code) N/A | |
| a. REPORT Unclassified | b. ABSTRACT Unclassified | c. THIS PAGE Unclassified | | | | |

Table of Contents

| | |
|--|-----------|
| LIST OF FIGURES | iv |
| LIST OF TABLES | v |
| EXECUTIVE SUMMARY | 1 |
| 1 SENSITIVITY METHODS PROBABILITY-OF-FAILURE ESTIMATES WITH RESPECT TO POD CURVE PARAMETERS | 2 |
| 1.1 INTRODUCTION | 2 |
| 1.2 METHODOLOGY DEVELOPMENT | 2 |
| 1.3 RESULTS AND DISCUSSION | 4 |
| 1.3.1 NUMERICAL EXAMPLE | 4 |
| 2 COMPLEX VARIABLE METHODS FOR SENSITIVITY ANALYSIS | 9 |
| 2.1 INTRODUCTION | 9 |
| 2.2 METHODOLOGY DEVELOPMENT | 9 |
| 2.2.1 NUMERICAL DIFFERENTIATION | 10 |
| 2.3 RESULTS AND DISCUSSION | 12 |
| 2.3.1 NUMERICAL EXAMPLE: THICK WALLED CYLINDER | 12 |
| 2.3.2 NUMERICAL EXAMPLE: DISC IN DIAMETRICAL COMPRESSION | 18 |
| 2.3.3 NUMERICAL EXAMPLE: SENSITIVITY OF STRESS INTENSITY FACTOR WITH RESPECT TO CRACK LENGTH | 24 |
| 3 PROBABILISTIC SENSITIVITY ANALYSIS WITH RESPECT TO BOUNDS OF TRUNCATED DISTRIBUTIONS | 35 |
| 3.1 METHODOLOGY | 35 |
| 3.2 RESULTS AND DISCUSSION | 37 |
| 3.2.1 NUMERICAL EXAMPLE | 37 |
| 4. CONCLUSIONS | 42 |
| 4.1 CONCLUSIONS | 42 |
| 4.2 CONCLUSIONS | 42 |
| 4.3 CONCLUSIONS | 43 |
| 5. RECOMMENDATIONS | 45 |
| 6. REFERENCES | 46 |
| LIST OF ACRONYMS, ABBREVIATIONS, AND SYMBOLS | 48 |

List of Figures

| | | |
|----|---|----|
| 1 | Normalized Probability-of-Failure with and without Inspection..... | 6 |
| 2 | Single inspection case: probability-of-failure with respect to μ_1 | 7 |
| 3 | Single inspection case: probability-of-failure with respect to σ_1 | 8 |
| 4 | Convergence of the Error in the Radial and Tangential Stress Models for Thick Walled Cylinder. A. The norm of the error in the radial stress, B. The norm of the error in the tangential stress | 13 |
| 5 | The Numerical Solution of the Radial and Tangential Stresses for Example 1..... | 14 |
| 6 | The Error in the First Order Sensitivity of the Radial Stress for Example 1 | 16 |
| 7 | The Error in the Second Order Sensitivity of the Radial Stress to the Inner Radius for Example 1. | 17 |
| 8 | The Finite Element Solution for the Stresses in a Disc in Diametrical Compression . | 20 |
| 9 | The Error in σ_x for Three Different Meshes for a Disc in Diametrical Compression | 21 |
| 10 | The Error in the First Order Sensitivity for a Disc in Diametrical Compression | 22 |
| 11 | The Error in the Second Order Sensitivity for a Disc in Diametrical Compression.... | 23 |
| 12 | The Four Problems Modeled for Example 3, A) Single Edge Crack (SENT)..... | 25 |
| 13 | Schematic of "Spider Web" Finite Element Mesh Used for J Integral Calculations... | 28 |
| 14 | Schematic of the Effect of Perturbing only the Nodes Along the Crack Face | 29 |
| 15 | Schematic of Rigid Body Perturbation of Nodes Around the Crack Tip | 30 |
| 16 | CFEM and ABAQUS Infinite Array Stress Intensity Factor (K) Accuracy vs. J integral domain | 32 |
| 17 | Imaginary Displacement Method Influence on K' Accuracy, Infinite Array, $h/h_1 = 10^{-6}$, CFEM K' within 30% of Reference..... | 33 |
| 18 | Imaginary Displacement Method Influence on K' Accuracy, Infinite Array, $h/h_1 = 10^{-6}$, CFEM K' within 0.5% of Reference | 33 |
| 19 | Accuracy of K and K' over a wide range of Complex Step Size | 34 |
| 20 | Descriptions of Velocity and Unit Normal Along Bounds..... | 36 |
| 21 | Flux of the JPDF in the Failure Region over the Surface S | 37 |
| 22 | 95% confidence limits (100 trials) for $\partial \mathcal{P}_f / \partial a$ as a function of the number of samples in \log_{10} scale (dashed - finite difference; solid – flux based) | 39 |

List of Tables

| | | |
|----|--|----|
| 1 | Input Parameters for Example Problem | 5 |
| 2 | The Norm of the Error in the Stress Solutions for a Thick Walled Cylinder | 14 |
| 3 | The Computational Time Required to Solve each Model for a Thick Walled Cylinder..... | 15 |
| 4 | The Norm of the Error in the Sensitivity of the Stress to the Inner Radius for a Thick Walled Cylinder | 15 |
| 5 | The Norm of the Error in the First Order Sensitivity of the Radial Stress as a Function of the Number of Elements for a Thick Walled Cylinder | 18 |
| 6 | The Norm of the Error in the First and Second Order Sensitivities of the Radial Stress as a Function of Step Size for a Thick Walled Cylinder | 18 |
| 7 | The Norm of the Error in the Stress Solutions for a Disk under Diametrical Compression..... | 21 |
| 8 | The Computational Time Required to Solve each Model for a Disk under Diametrical Compression | 22 |
| 9 | The Norm of the Error in the First Order Sensitivity of σ_x as a Function of the Number of Elements for a Disk under Diametrical Compression..... | 24 |
| 10 | The Norm of the Error in the First and Second Order Sensitivities of the Radial Stress as a Function of Step Size for a Disk under Diametrical Compression. | 24 |
| 11 | Reference Formulas for the Stress Intensity Factor (K) | 26 |
| 12 | The First Partial Derivative of Each Reference Formula with Respect to Crack Length | 27 |
| 13 | Parameters of the Plane Strain Problems Investigated | 27 |
| 14 | Selected Finite Element Model Characteristics | 28 |
| 15 | Typical Computation Times | 29 |
| 16 | Accuracy of K and K' for Four Methods of Imaginary Displacement for the Infinite Array Problem, J-Integration Domain 36, $h/h_1 = 10^{-6}$ | 31 |
| 17 | Probabilistic Sensitivity Results for Limit State $g = r - s$ (R Standard Normal, S Uniform)..... | 38 |
| 18 | Variance of sensitivity estimates $\partial \mathcal{P}_f / \partial \theta$ as a function of sampling correlation (100 trials) – actual correlation in parentheses | 40 |
| 19 | Coefficient of Variation (100 Trials) of Sensitivities with respect to Bounds as a Function of the Number of Samples..... | 41 |

Executive Summary

Probabilistic engine health management (PHM) is expected to be a go-forward approach for the USAF and other DoD agencies to enable dramatic improvements in the assessment and management of military assets. As a result, accurate and information-rich probabilistic lifing methods are essential to assess the benefits of technology insertion programs for PHM.

The objective of this research was threefold: 1) to enhance probabilistic lifing methods to provide new information regarding the sensitivity of probabilistic lifing estimates with respect to non-destructive inspection methods, material parameters, loading, stress levels, etc., 1) to address computational efficiency issues such that application of the enhancements are practical, and 3) to integrate the new methods with existing approaches as permissible to foster adoption.

Three major tasks were undertaken: 1) develop sensitivity methods for lifing scenarios with simulated inspections processes, 2) explore new complex variable methods for sensitivity analysis, and 3) enhance the score function method to address new scenarios.

In each case significant research was accomplished that lead to several enhancements. In particular: 1) a new probabilistic sensitivity method was developed that will compute the partial derivative of the probability-of-failure with respect to the parameters of a Probability-of-Detection (POD) curve for negligible cost, 2) new complex-variable sensitivity methods were developed and exploited to determine shape sensitivities for finite element models (particularly with respect to crack size) in a highly accurate manner and to solve initial value differential equations with extreme accuracy, and 3) a new method to compute probabilistic sensitivities with respect to bounds of truncated distributions was developed and tested.

Ancillary objectives were also accomplished. In particular, four students were supported wholly or in part in obtaining a Masters of Science in Mechanical Engineering, 4 conference papers were submitted and presented, 1 journal paper was published, 2 journal papers are under review, and 4 Matlab-based software programs were provided to AFRL for technology transition. The software programs consisted of a) a generic probabilistic sensitivity module, b) a weight function-based fatigue lifing code, c) an inspection sensitivity program, and d) complex-variable finite element code for shape sensitivity analysis.

1 Sensitivity methods probability-of-failure estimates with respect to POD curve parameters

1.1 Introduction

Nondestructive evaluation (NDE), also known as nondestructive testing (NDT) or nondestructive inspection (NDI), plays a vital role in fracture control plans. Methods such as visual, dye penetrant, ultrasonics, radiography, and eddy current are among the common inspection techniques used to ensure structural integrity [1]. The type of inspection and the times of inspection must be carefully selected to ensure safety with reasonable cost. There are a number of industries that have a long history of application of NDE methods for structural integrity. For example, applications include nuclear [2-4], petroleum [5], aircraft structures [6-8], gas turbines [9-10], and offshore structures [11] to name a few. Rummel et al. [12] provide a summary of a number of issues related to the application of NDE methods to systems.

The inspection process is simulated using a Probability of Detection (POD) curve that quantifies the probability of detecting a crack as a function of the crack size. A probabilistic life analysis integrates probability distributions of crack sizes, load, geometries, and material properties with the inspection processes to determine the probability-of-failure with and without inspection. The purpose is to ensure a sufficient level of reliability in the structure and to optimize the inspection process for cost and maintenance-related issues.

However, there is always some doubt as to the correct values for the parameters of a POD curve for a particular field application due to the mismatch of the environment for development of the POD curve versus its field application. In addition, there may be value in “what-if” scenarios to quickly assess the value of changes in the inspection method in reducing the POF or reducing the cost of inspections. As a result, it is useful to have a quantitative estimate how the probability-of-failure varies as a function of the parameters of a particular POD curve. Therefore, a methodology was derived that provides a convenient low-cost means to calculate the POF sensitivities, that is, the partial derivative $\partial P_f / \partial \theta$, where P_f is the probability-of-failure and θ is any parameter of a POD curve.

1.2 Methodology Development

The basic methodology is summarized here for a single inspection. A generalization to more inspections can be found in [13].

The probability-of-failure is determined by evaluating the integral

$$P_f(t) = \int_{-\infty}^{\infty} I(\mathbf{x}, t) f_{\mathbf{x}}(\mathbf{x}) d\mathbf{x} \quad (1)$$

where \mathbf{x} defines a vector of random variables such as initial crack size, external load, crack growth rate, fracture toughness, $f_{\mathbf{x}}$ represents the joint probability density function of the random variables, and $I(\mathbf{x}, t)$ denotes an indicator function such that

$$I(\mathbf{x}, t) = \begin{cases} 0 & g(\mathbf{x}, t) > 0 \quad \text{safe} \\ 1 & g(\mathbf{x}, t) \leq 0 \quad \text{fail} \end{cases} \quad (2)$$

For a lifing analysis, $g(\mathbf{x}, t)$ is usually defined as $g(\mathbf{x}, t) = t_f - t_0$, where t_f is the computed cycles to failure and t_0 is a user-defined limit. Using this definition of g , the probability-of-failure is the probability of the structural component failing before the user-defined time t_0 .

The probability-of-failure with an inspection can be determined by evaluating the integral

$$P_f(t) = \int_{-\infty}^{\infty} I(\mathbf{x}, t) (1 - \text{POD}(\boldsymbol{\theta}, a(\mathbf{y}, t_1))) f_{\mathbf{x}}(\mathbf{x}) d\mathbf{x} \quad t > t_1 \quad (3)$$

where t_1 denotes the time of inspection 1, a represents the crack size, and \mathbf{y} represents the random variables that affect the crack size; \mathbf{y} is a subset of \mathbf{x} . The sensitivity of the POF with respect to parameters of the POD curve ($\boldsymbol{\theta}$) can be determined by taking the derivative of Equation 3 and rearranging to yield

$$\frac{\partial P_f(t)}{\partial \boldsymbol{\theta}_1} = \begin{cases} 0 & t \leq t_1 \\ \int_{-\infty}^{\infty} I(\mathbf{x}, t) \Omega_1(\boldsymbol{\theta}_1, a(\mathbf{y}, t_1)) \text{CPOD}_1(\boldsymbol{\theta}_1, a(\mathbf{y}, t_1)) f_{\mathbf{x}}(\mathbf{x}) d\mathbf{x} & t > t_1 \end{cases} \quad (4)$$

where $\Omega_q(\boldsymbol{\theta}_q, a(\mathbf{y}, t_q)) = -\frac{\partial \text{POD}_q(\boldsymbol{\theta}_q, a(\mathbf{y}, t_q))}{\partial \boldsymbol{\theta}_q} \frac{1}{\text{CPOD}_q(\boldsymbol{\theta}_q, a(\mathbf{y}, t_q))}$. The derivative

$\partial \text{POD}_q(\boldsymbol{\theta}_q, a(\mathbf{y}, t_q)) / \partial \boldsymbol{\theta}_q$ can be computed analytically given an analytical definition of the POD curve.

The sensitivity $\partial P_f / \partial \boldsymbol{\theta}$ can be approximated in the same manner as estimating the probability-of-failure using sampling as

$$\frac{\partial P_f(t)}{\partial \boldsymbol{\theta}_1} \approx \begin{cases} 0 & t \leq t_1 \\ \frac{1}{N} \sum_{i=1}^{N_1} I(\mathbf{x}_i, t) \Omega_1(\boldsymbol{\theta}_1, a(\mathbf{y}_i, t_1)) & t > t_1 \end{cases} \quad (5)$$

where $\boldsymbol{\theta}_1$ represents the vector of parameters of POD_1 , N_1 denotes the samples that reach inspection 1, i.e., have not failed before t_1 nor detected, $a(\mathbf{y}_i, t_1)$ denotes the crack size at time t_1 , \mathbf{y}_i represents the random variables that affect crack size for realization i , \mathbf{x}_i represents all the random variables for realization i , and N denotes the total number of samples in the simulation. Note, the summation in Equation 5 is divided by N instead of N_1 in order to provide the sensitivity with respect to the total samples N .

1.3 Results and Discussion

A new sensitivity method has been developed that can provide accurate partial derivatives of the probability-of-failure with respect to the parameters of a POD curve. The accuracy of the sensitivities was verified by comparison with finite difference estimates on several numerical examples. The new method computes the sensitivity using the same samples used to calculate the probability-of-failure, hence the cost is negligible. In contrast, the finite difference approach is extremely laborious in that a new probabilistic analysis must be conducted for each sensitivity and a large number of samples is required for accuracy.

1.3.1 Numerical Example

An academic example is presented to demonstrate the methodology. The example presumes a defect exists, thus, the POF has been normalized to 1. The problem is fictitious but serves to demonstrate the elements of the method using an easy to understand problem. The problem consists of an edge through crack growing in a semi-infinite rectangular plate under constant amplitude loading. The initial crack size and material properties are representative of titanium, however, the POD curve is contrived. Four random variables were considered: initial crack size (lognormal), Paris crack growth constants C and n (correlated normal) and fracture toughness (normal). The problem parameters are given in Table 1. The random variable vector \mathbf{X} consists of $\mathbf{X} \in a_i, C, n, K_{IC}$, and the \mathbf{Y} vector of random variables consists of $\mathbf{Y} \in a_i, C, n$.

For this crack geometry using the Paris crack growth law, the crack size as a function of cycles a , the critical crack size a_c , the cycles-to-failure t_f , the crack size a_q at any time of inspection t_q , and the limit state $g(\mathbf{x}, t)$ can be determined in closed form as shown below.

$$da/dt = C(\Delta K)^m \quad (6)$$

$$K_I = 1.12\sigma_{\max} \sqrt{\pi a} \quad (7)$$

$$a_c = (K_{IC} / (1.12\sigma_{\max} \sqrt{\pi}))^2 \quad (8)$$

$$t_f = \frac{2}{(m-2)C(1.12\Delta\sigma\sqrt{\pi})^m} \left(\frac{1}{a_i^{(m-2)/2}} - \frac{1}{a_c^{(m-2)/2}} \right) \quad (9)$$

$$a_q = \left(\frac{1}{a_i^{(m-2)/2}} - t_q \frac{(m-2)C(1.12\Delta\sigma\sqrt{\pi})^m}{2} \right)^{2/(2-m)} \quad (10)$$

$$g(\mathbf{x}, t) = t_f - t_0 \quad (11)$$

where t_0 is a specified number of cycles.

The values used in the analysis are shown in Table 1. For this problem, the initial crack size, Paris constants and the fracture toughness were random.

Table 1 Input Parameters for Example Problem

| | |
|--------------------------------|---------------------------------|
| ΔK | $1.12\Delta\sigma\sqrt{\pi a}$ |
| $\Delta\sigma(=\sigma_{\max})$ | 675MPa |
| K_{IC} | $N[55,5.5] \text{ MPa}\sqrt{m}$ |
| ρ_{Cm} | -0.9751 |
| $\text{Log}_{10}(C)$ | $N[-11.8,0.157]$ |
| m | $N[3.81,0.146]$ |
| a_i | $L[15.1,8.48] \mu m$ |

A single inspection was simulated at 10,000 cycles using a lognormal POD of the form

$POD(a) = \frac{1}{2} + \frac{1}{2} \text{Erf}\left[\frac{\ln[a] - \mu}{\sqrt{2}\sigma}\right]$ with parameters $\mu_1 = -9, \sigma_1 = 0.8$. The normalized POF as a

function of cycles with and without inspection is shown in Figure 1. The sensitivity of the probability-of-failure with respect to μ_1 and σ_1 as a function of cycles is given in Figures 2 and 3, respectively, with the solid (red) line denoting the results using the equations developed here and finite difference results denoted by the dotted (black) points. One million samples were used for the calculation. The results indicate a very good agreement with the finite difference solutions verifying the accuracy of the methodology. Finite difference sensitivity estimates require a separate reanalysis of the POF using a perturbed value of μ_1 and σ_1 (2 additional analyses), e.g., $\partial P_f / \partial \mu_1 \approx \Delta P_f / \Delta \mu_1 = (P_f(\mu_1 + \Delta \mu_1) - P_f(\mu_1)) / \Delta \mu_1$. A large number of samples must be used to ensure that the sampling variance is sufficiently small to accurately estimate the difference between two near-equal probabilities. Also, the accuracy is dependent upon the value chosen for $\Delta \mu_1$. As a result, the finite difference operations are costly since they require multiple analyses and a large number of samples. Conversely, using the methodology presented here, all sensitivities are obtained from a single analysis through post-processing.

The results for a single inspection shown here generalize to any number of inspections with similar accuracy. For multiple inspections, methodologies to address two cases were developed and demonstrated: different POD curves used during for the inspections, and b) the same POD curved used for all inspections.

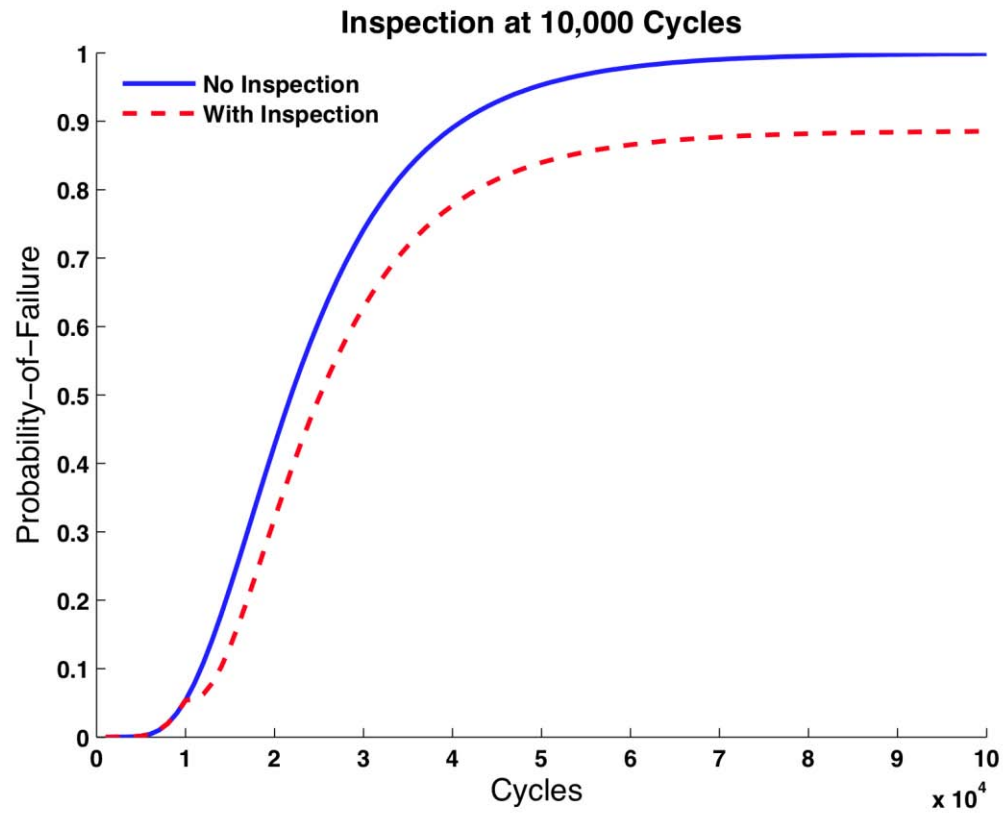


Figure 1 Normalized Probability-of-Failure with and without Inspection

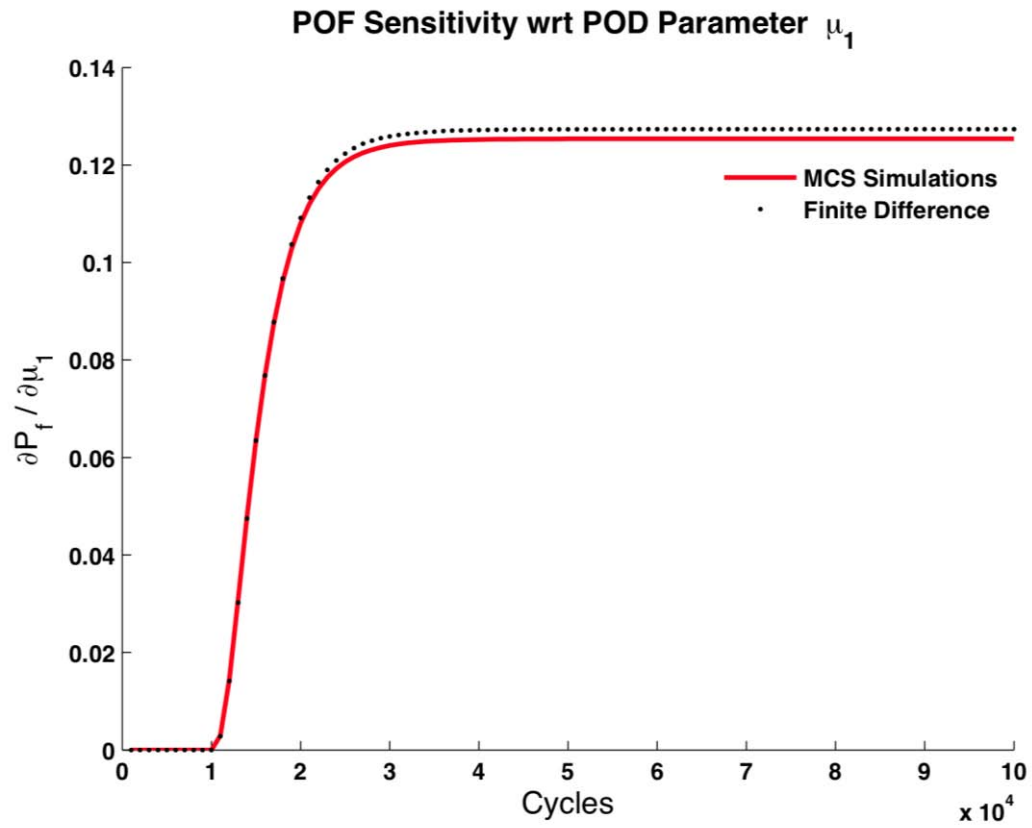


Figure 2 Single Inspection Case: Probability-of-Failure with respect to μ_1

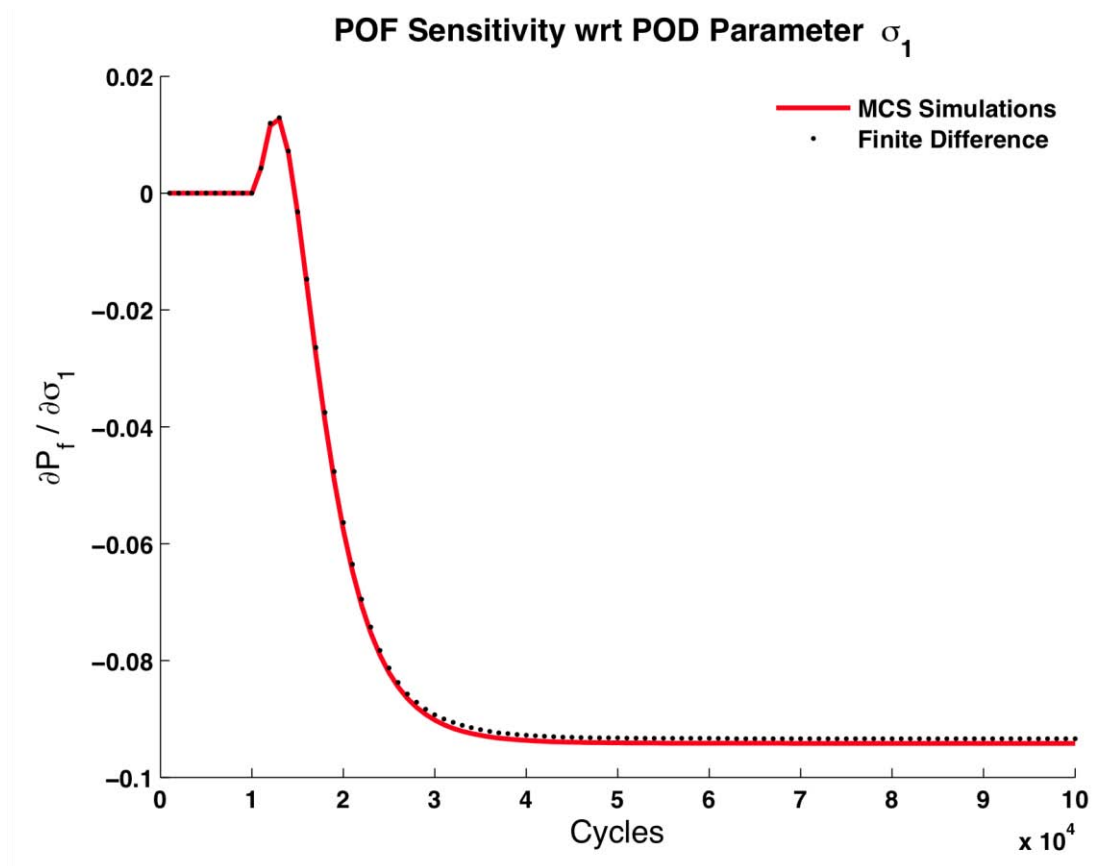


Figure 3 Single Inspection Case: Probability-of-Failure with respect to σ_1

2 Complex Variable Methods for Sensitivity Analysis

2.1 Introduction

Shape sensitivity analysis of finite element models is useful for optimization and design modifications. The use of complex variable methods for shape sensitivity analysis has some potential advantages over other methods. In particular, implementation for first order sensitivities is straightforward as the only additional requirement is the analysis of a finite element model containing a perturbation of the finite element mesh along the imaginary axis, that is, the real valued coordinates of the mesh are unaltered. Higher order sensitivities can be determined using analyses with perturbations along the real and imaginary axes. Although simple in concept, standard finite element codes (including commercial ones) do not allow complex variable nodal coordinates, hence, special purpose codes were developed under this program. The methodology is demonstrated using a two dimensional finite element model on problems with known analytical solutions. It is found that the error in the sensitivities is primarily defined by the error in the finite element solution, not the error in the sensitivity method.

2.2 Methodology Development

Sensitivities, otherwise known as partial derivatives, are easily calculated through finite differencing methods. Finite differencing requires that a function be evaluated at additional sample points along the real axis and the derivative of the function estimated by calculating the relative difference in the function's value divided by the difference in the sample points.

Over the last twenty years, alternative numerical differentiation techniques have emerged for use in sensitivity analysis. Two of these methods are complex variable based: the complex Taylor series expansion (CTSE), also referred to as the complex step derivative method, and Fourier differentiation (FD). These methods offer more accurate and stable derivatives compared to finite differencing.

CTSE was first described by Lyness and Moler in the late 1960's [14,15]. It reemerged as a tool for engineering analysis with a paper by Squire and Trapp in 1998 [16]. Since then it has been used in a wide variety of engineering fields including computational fluid dynamics, dynamic system optimization and others [17-24]. In all of these fields, CTSE has offered a significant improvement in accuracy over standard finite differencing methods.

Fourier differentiation was also developed by Lyness in the late 60's and early 70's [14,15,25]. The method was further described by Henrici and more recently Bagley [26,27]. The method utilizes additional sample points in the complex plane and an FFT routine to calculate derivatives including high order derivatives with exceptional accuracy. To date, the method has not been widely used for the determination of sensitivities for engineering problems.

2.2.1 Numerical Differentiation

Numerical differentiation is a process through which an estimate of a function's derivative can be obtained. A derivative is defined as the limit of the change in a function's value across two different points as the distance between the two points goes to zero.

$$f'(x_o) = \lim_{x \rightarrow x_o} \frac{f(x) - f(x_o)}{x - x_o} \quad (12)$$

Finite differencing methods estimate derivatives by approximating the limit in Equation 12 as a difference between a function evaluated at two distinct points located a distance h apart divided by h .

$$f'(x_o) \approx \frac{f(x_o + h) - f(x_o)}{h} \quad (13)$$

This distance, h , is often called the step size. When h is positive, the method is referred to as forward differencing. When h is negative it is called backwards differencing. When the forward difference and the backwards difference results are averaged, the method is called central differencing (CD). The equation for central differencing is as follows.

$$f'(x_o) \approx \frac{f(x_o + h) - f(x_o - h)}{2h} \quad (14)$$

The approximation of the derivatives as a difference between two nearly-equal numbers leads to error due to the truncation of terms in the function's Taylor series. This error can be eliminated by making the step size as small as possible. However, as the step size gets very small, a new source of error arises. This new error is round-off error and it is due to the fact that a computer cannot accurately calculate a small difference between two near-equal numbers. This means that for finite differencing there is a lower limit on the step size and also a limit on the maximum achievable accuracy.

For the forward differencing method, all Taylor series terms above the first order term are ignored. This means that the order of accuracy for a given step size is $O(h)$. Using CD, all the even order terms in the Taylor series cancel and the accuracy of the method becomes $O(h^2)$.

Higher order derivatives can also be calculated through CD by using additional sample points. The formula for the second derivative is.

$$f^{(2)}(x_o) \approx \frac{f(x_o + h) - 2f(x_o) + f(x_o - h)}{h^2} \quad (15)$$

where the superscript (2) denotes the second derivative.

One of the problems with CD is that the calculation of higher order derivatives requires more sample points and more difference operations. Each additional difference operation results in an increase in the round-off error, which further restricts the lower limit of h . This means that CD is not a good choice for the calculation of higher order derivatives.

CTSE is another numerical differentiation method similar in concept to finite differencing. CTSE uses the orthogonality of the real and imaginary axes of the complex plane to calculate derivatives with fewer difference operations and in turn less round-off error when compared to CD. Similar to finite differencing, CTSE requires the difference of two analyses but with a small perturbation along the imaginary axis. That is, variable $X = x_0$ is perturbed to $X = x_0 + ih$, where i denotes an imaginary number and h denotes the step size. The formulae for the derivatives can be derived from the Taylor series representation of the function evaluated at the complex sample point.

$$f(x_0 + ih) = f(x_0) + f^{(1)}(x_0) \frac{ih}{1!} + f^{(2)}(x_0) \frac{(ih)^2}{2!} + f^{(3)}(x_0) \frac{(ih)^3}{3!} + \dots \quad (16)$$

where $f^{(1)}$ denotes the first derivative, $f^{(2)}$ the second, etc. Taking the imaginary part of both sides of Equation 16 and solving for the first derivative will result in an approximation with accuracy $O(h^2)$.

$$f^{(1)}(x_0) \approx \frac{f(x_0 + ih) - f(x_0)}{h} \approx \frac{\text{Im}(f(x_0 + ih))}{h} \quad (17)$$

It is noted that no difference operation is needed for the first derivative. This means that the step size can be made arbitrarily small with no concern about increasing round-off error. Taking the real part of Equation 16, the formula for the second derivative with error $O(h^2)$ can be derived.

$$f^{(2)}(x_0) \approx \frac{2(f(x_0) - \text{Re}(f(x_0 + ih)))}{h^2} \quad (18)$$

It is noted that the second derivative contains a difference operation meaning that round-off error will be a problem if h is set too small. By using more sample points along the imaginary axis it is possible to solve Equation 16 to obtain the higher order derivatives [28].

Higher order derivatives can be computed using complex variable sensitivity method such as Fourier Differentiation (FD) [27]. The heart of Fourier differentiation is making a real valued function become a periodic complex function. This is accomplished by adding a periodic, oscillatory, complex component to each of the function's real independent variables. The resulting periodic function now has a Taylor series representation that takes on the properties of a periodic Fourier series. Fast Fourier transform techniques are used to determine the coefficients of this series. The resulting coefficients contain the function's derivatives.

A central feature of Fourier differentiation is to make the individual terms in the Taylor series oscillate at different frequencies. To achieve these oscillations, the perturbation to the variable x is taken to be a complex number as $\Delta x = ce^{-i\theta}$, where c is a sampling radius. This expression extracts from the series the n^{th} coefficient that contains the n^{th} derivative of the function,

$$\frac{1}{2\pi} \int_{-\infty}^{\infty} f(x_o + ce^{-i\theta}) e^{in\theta} d\theta = \frac{f^{(n)}(x_o) c^n}{n!} \quad (19)$$

If the function of interest is evaluated at N sample points along a circular contour c in the complex plane centered on the initial point, a vector of the sampled data can be run through an FFT routine and the output will be the first N terms in the function's Taylor series. The n^{th} order derivative of the function can then be calculated from the Taylor series coefficients by using the following relationship.

$$f^{(n)}(z_o) = \frac{a_n n!}{c^n} \quad (20)$$

where a_n is the n^{th} Taylor series coefficient. For more information on Fourier differentiation see ref. [27].

2.3 Results and Discussion

2.3.1 Numerical Example: Thick Walled Cylinder

Two problems with analytical solutions were examined in order to test the accuracy of the three numerical differentiation techniques; a thick walled cylinder under uniform boundary pressure and a disk under diametrical compression. The equations that govern the stress through the thickness of the cylinder are given in Equation 21 [29],

$$\begin{aligned} \sigma_r &= \frac{r_1^2 r_2^2 p}{r_2^2 - r_1^2} \frac{1}{r^2} - \frac{r_2^2 p}{r_2^2 - r_1^2} \\ \sigma_\theta &= -\frac{r_1^2 r_2^2 p}{r_2^2 - r_1^2} \frac{1}{r^2} - \frac{r_2^2 p}{r_2^2 - r_1^2} \end{aligned} \quad (21)$$

where, r_1 is the inner radius, r_2 is the outer radius, and p is the boundary pressure. For this example, the inner radius of the cylinder is 0.5 m, the outer radius is 1 m and the boundary pressure is 10 kPa. The stress equations given in Equation 21 can be differentiated with respect to the inner radius to generate the sensitivities of the stresses. The first and second order sensitivities of the stresses with respect to the inner radius appear in Equations 22 and 23.

$$\frac{\partial \sigma_r}{\partial r_1} = 2 \left[\frac{r_1 r_2^2 p}{(r_2^2 - r_1^2)^2} \left(\frac{r_2^2}{r^2} - 1 \right) \right] \quad (22)$$

$$\frac{\partial \sigma_\theta}{\partial r_1} = -2 \left[\frac{r_1 r_2^2 p}{(r_2^2 - r_1^2)^2} \left(\frac{r_2^2}{r^2} + 1 \right) \right]$$

$$\frac{\partial^2 \sigma_r}{\partial r_1^2} = 2 \left[\frac{(3r_1 + r_2^2) r_2^2 p}{(r_2^2 - r_1^2)^3} \left(\frac{r_2^2}{r^2} - 1 \right) \right] \quad (23)$$

$$\frac{\partial^2 \sigma_\theta}{\partial r_1^2} = -2 \left[\frac{(3r_1 + r_2^2) r_2^2 p}{(r_2^2 - r_1^2)^3} \left(\frac{r_2^2}{r^2} + 1 \right) \right]$$

This problem was solved using four different meshes in order to examine the convergence of the error in the solution. The coarsest mesh contained 888 elements and 1868 nodes; the next mesh contained 1792 elements and 3716 nodes; the third mesh contained 6184 elements and 12,608 nodes; and the finest mesh consisted of 25,124 elements and 50,724 nodes. The solutions for the radial and tangential stresses as calculated using the 6184 element mesh are shown in Figure 4.

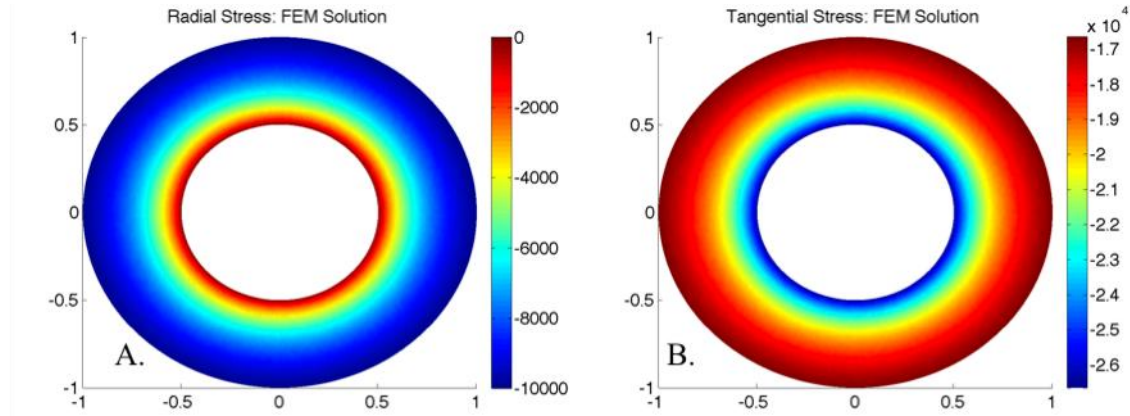


Figure 4. The Numerical Solution of the Radial and Tangential Stresses for Example 1. A) The FEM Solution for the Radial Stresses B) The FEM Solution for the Tangential Stresses

The following norm was selected in order to compare the error in the four different mesh cases.

$$\|error\| = \frac{mean(|\sigma_{analytical} - \sigma_{numerical}|)}{mean(|\sigma_{analytical}|)} \quad (24)$$

Table 2 shows the norm of the error in both the radial and tangential stress solutions for each mesh case. This data is shown graphically in Figure 5. It is seen that each successive mesh iteration reduces the error by approximately half an order of magnitude.

Table 2. The Norm of the Error in the Stress Solutions for a Thick Walled Cylinder

| Number of Elements | Radial Stress | Tangential Stress |
|--------------------|---------------|-------------------|
| 888 | 5.251E-3 | 3.1852E-3 |
| 1792 | 2.626E-3 | 1.7412E-3 |
| 6184 | 7.574E-4 | 5.3097E-4 |
| 25124 | 1.860E-4 | 1.3248E-4 |

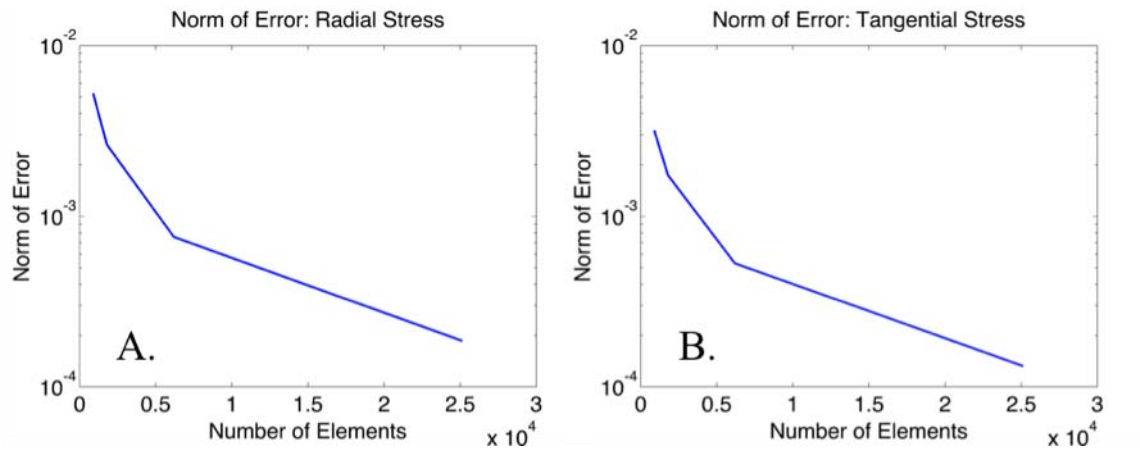


Figure 5. Convergence of the Error in the Radial and Tangential Stress Models for Thick Walled Cylinder. A. The Norm of the Error in the Radial Stress, B. The Norm of the Error in the Tangential Stress

The amount of computational time (wall time) needed to solve each finite element model is shown in Table 3. Given the amount of computational time required for the 25,124 element case and the fact that the complex sensitivity solutions will require three times more computation than the real valued case, the 6184 element case was used to generate the first, second and third order sensitivities. For each sensitivity method the step size or sampling radius was 0.001, which is approximately $1/30^{\text{th}}$ of the average element edge length. CTSE and CD were both performed using as few sample points as possible, and FD was performed using 6 sample points.

Table 3. The Computational Time Required to Solve each Model for a Thick Walled Cylinder

| Number of Elements | Time For Solution (s) |
|--------------------|-----------------------|
| 888 | 8.49 |
| 1792 | 19.48 |
| 6184 | 130.76 |
| 25124 | 2799.77 |

The pointwise error in the first and second order sensitivities is shown in Figure 6 and 7, respectively using the following formula,

$$error = \frac{\sigma_{analytical} - \sigma_{numerical}}{\max(|\sigma_{analytical}|)} \quad (25)$$

This formula was chosen so as to minimize the influence of large errors at locations where the solution is near zero such as at the inner radius for the radial stress.

The norm of the error in the first, second, and third order sensitivities appears in Table 4. The error in the first order sensitivities of the radial stress over the entire domain appear in Figure 6, and the error in the second order sensitivities of the radial stress appear in Figure 7. These figures show only very slight differences between the three methods. It is also seen that along the inner circumference of the cylinder the error is large. This is due to the fact that the sensitivity cannot be accurately calculated on the inner radius because the boundary conditions require the solution to be fixed at the inner surface.

Table 4. The Norm of the Error in the Sensitivity of the Stress to the Inner Radius for a Thick Walled Cylinder

| Method | Radial Stress | | | Tangential Stress | | |
|--------|---------------|-----------|-----------|-------------------|-----------------|-----------|
| Order | 1st | 2nd | 3rd | 1st | 2 nd | 3rd |
| CD | 4.7265E-2 | 8.1689E-2 | 2.4292E-2 | 8.4286E-2 | 3.2213E-1 | 1.4765E-2 |
| CTSE | 4.7268E-2 | 8.1766E-2 | 2.4298E-2 | 8.2488E-2 | 3.1587E-1 | 1.4769E-2 |
| FD | 4.7268E-2 | 8.1671E-2 | 2.4295E-2 | 8.7353E-2 | 3.3258E-1 | 1.4769E-2 |

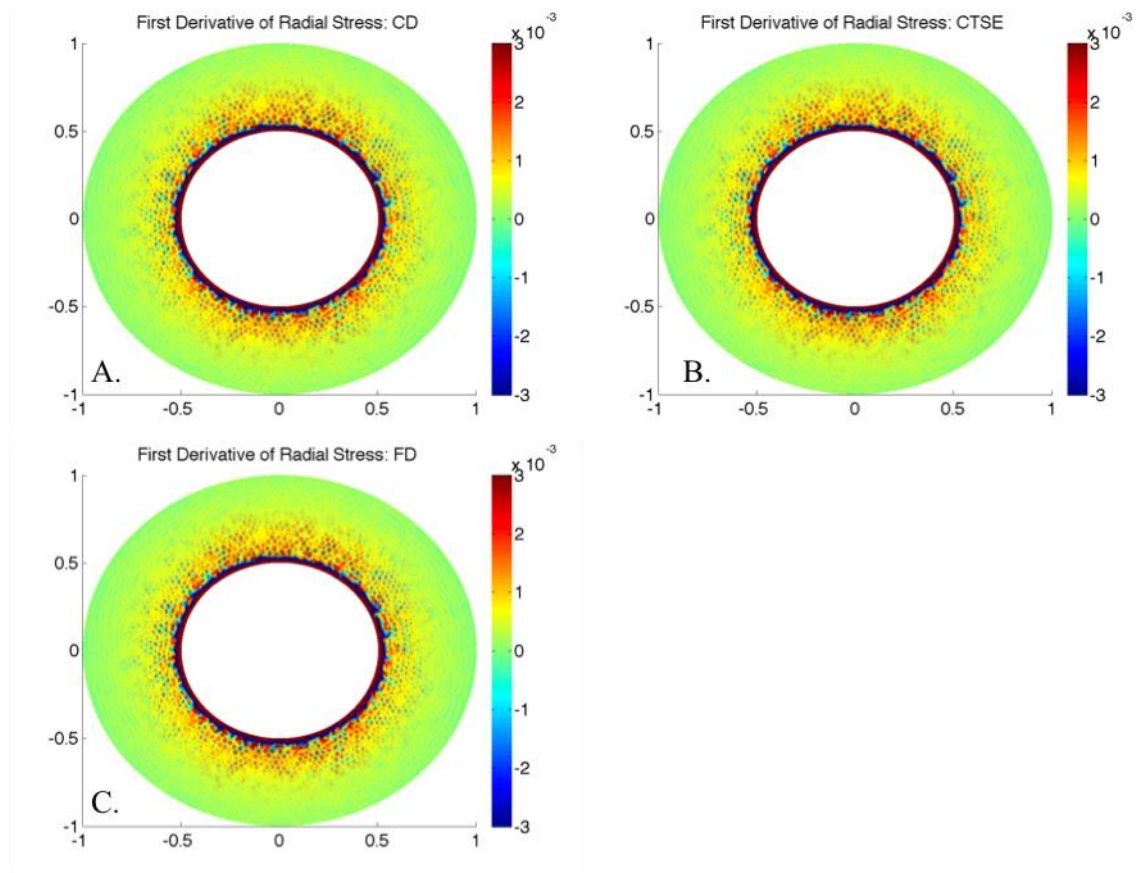


Figure 6. The Error in the First Order Sensitivity of the Radial Stress for Example 1. A) Error in CD, B) error in CTSE, C) error in FD.

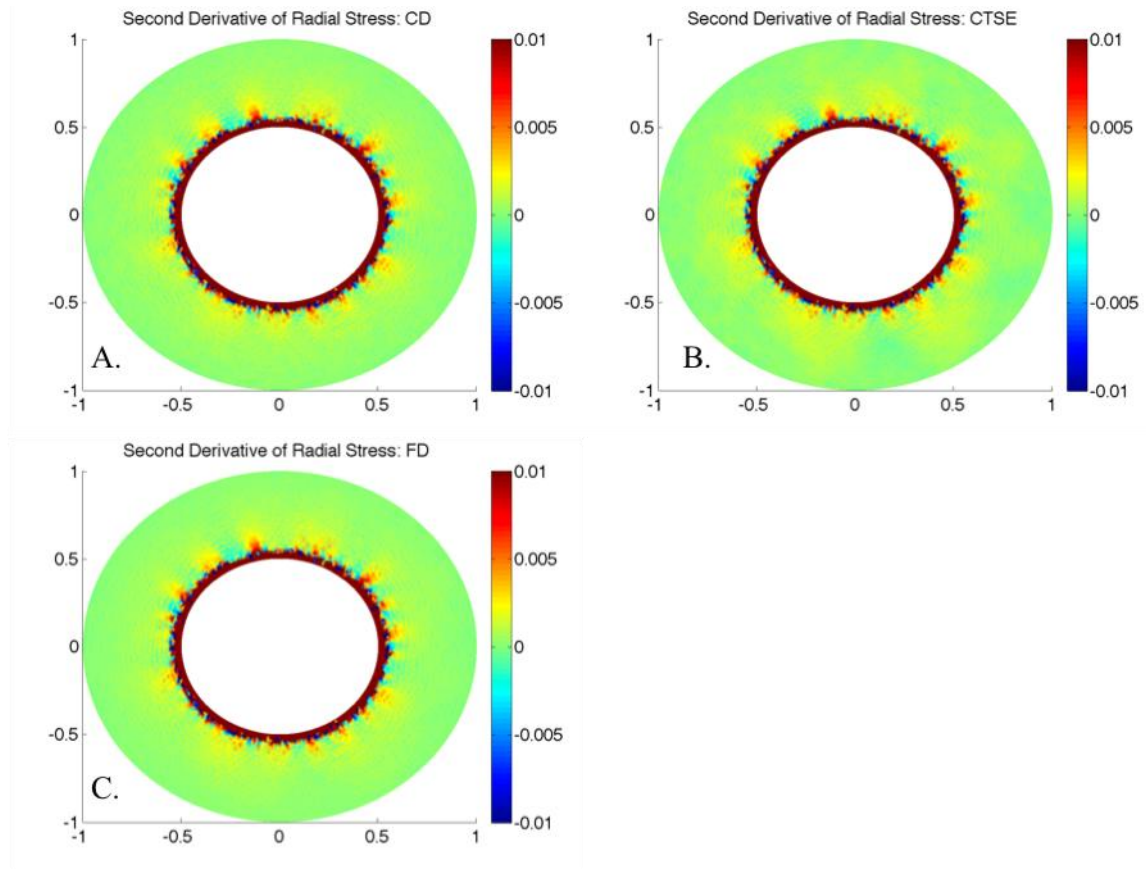


Figure 7. The Error in the Second Order Sensitivity of the Radial Stress to the Inner Radius for Example 1. A) Error in CD, B) error in CTSE, C) error in FD.

The norm of the error in each case is mostly independent of the method selected. This is especially true for the first order sensitivities. The fact that the error is similar between all three methods points to the fact that the error in the solution is dominating errors arising from the differentiation methods themselves. This is seen by looking at the first and second order sensitivities of the radial stress as a function of the number of elements shown in Table 5. It is quickly seen that each additional mesh refinement increases the accuracy of the method. This reduction in the errors of the sensitivities is similar to the reduction in the error of the solution due to further mesh refinement seen in Table 2.

Table 5. The Norm of the Error in the First Order Sensitivity of the Radial Stress as a Function of the Number of Elements for a Thick Walled Cylinder

| Number of Elements | CD | | CTSE | | FD | |
|--------------------|-----------------|---------|---------|---------|---------|---------|
| Order | 1 st | 2nd | 1st | 2nd | 1st | 2nd |
| 888 | 1.27E-1 | 2.08E-1 | 1.27E-1 | 2.08E-1 | 1.27E-1 | 2.08E-1 |
| 1792 | 8.97E-2 | 1.53E-1 | 8.99E-2 | 1.52E-1 | 8.99E-2 | 1.52E-1 |
| 6184 | 4.72E-2 | 8.16E-2 | 4.72E-2 | 8.17E-2 | 4.72E-2 | 8.16E-2 |
| 25124 | 2.29E-2 | 4.00E-2 | 2.29E-2 | 4.00E-2 | 2.29E-2 | 3.98E-2 |

The error in the first and second order sensitivities of the radial stress calculated using three different step sizes is shown in Table 6. It is seen that changing the step size does not have much effect on the accuracy of the sensitivity. This is a further indicator that the accuracy of the solution is limiting the accuracy of the sensitivities, not the accuracy of the numerical differentiation methods. One exception is the second order sensitivity at the smallest step size, 0.0001 or 1/300th of the average element edge length. At this step size each method produces sensitivities that are less accurate than those calculated with a larger step size. This indicates that the machine round-off error associated with this step size may be similar in magnitude to the error due to the solution.

Table 6. The Norm of the Error in the First and Second Order Sensitivities of the Radial Stress as a Function of Step Size for a Thick Walled Cylinder

| Step Size | CD | | CTSE | | FD | |
|-----------|-----------|-----------|-----------|-----------|-----------|-----------|
| Order | 1st | 2nd | 1st | 2nd | 1st | 2nd |
| .0001 | 4.7268E-2 | 8.2959E-2 | 4.7268E-2 | 1.0500E-1 | 4.7268E-2 | 9.2942E-2 |
| .001 | 4.7265E-2 | 8.1689E-2 | 4.7268E-2 | 8.1766E-2 | 4.7268E-2 | 8.1671E-2 |
| .01 | 4.7091E-2 | 8.2920E-2 | 4.7249E-2 | 8.1197E-2 | 4.7271E-2 | 8.1748E-2 |

2.3.2 Numerical Example: Disc in Diametrical Compression

One of the classical tests in material analysis is the disc in diametrical compression [20]. In this test a circular disc is loaded in compression along its y-axis. The load is modeled as a point load. This loading and geometry generates a very nice uniform tensile stress along the x-axis of the specimen. It is thus useful in examining the tensile properties of a material without actually loading the specimen in tension. This test is also known as the indirect tensile test or the Brazil nut test.

The diametrical compression test has an analytical solution that can be derived through simple superposition. The solution of the stresses is given in Equation 26 [29].

$$\begin{aligned}
\sigma_x &= \frac{-2P}{\pi} \left[\frac{(R-y)x^2}{(x^2 + (R-y)^2)^2} + \frac{(R+y)x^2}{(x^2 + (R+y)^2)^2} - \frac{1}{2R} \right] \\
\sigma_y &= \frac{-2P}{\pi} \left[\frac{(R-y)^3}{(x^2 + (R-y)^2)^2} + \frac{(R+y)^3}{(x^2 + (R+y)^2)^2} - \frac{1}{2R} \right] \\
\tau_{xy} &= \frac{2P}{\pi} \left[\frac{(R-y)^2 x}{(x^2 + (R-y)^2)^2} + \frac{(R+y)^2 x}{(x^2 + (R+y)^2)^2} \right]
\end{aligned} \tag{26}$$

In these equations, P is the magnitude of the point load, R is the radius of the disc, and x and y specify the location at which the stress is calculated, with the point (0,0) located at the center of the disc. The analytic solutions of Equation 26 can be differentiated to yield the sensitivities with respect to the radius of the disc. The equations for the first two sensitivities of the normal stress in the x-direction with respect to the radius are

$$\begin{aligned}
\frac{d\sigma_x}{dR} &= \frac{2P}{\pi} \left[\frac{(3R^2 - 6Ry - x^2 + 3y^2)x^2}{(x^2 + (R-y)^2)^3} + \frac{(3R^2 + 6Ry - x^2 + 3y^2)x^2}{(x^2 + (R+y)^2)^3} + \frac{1}{2R^2} \right] \\
\frac{d^2\sigma_x}{dR^2} &= \frac{-2P}{\pi} \left[\frac{12(R-y)(R^2 - 2Ry - x^2 + y^2)x^2}{(R^2 - 2Ry + x^2 + y^2)^4} + \right. \\
&\quad \left. \frac{12(R+y)(R^2 + 2Ry - x^2 + y^2)x^2}{(R^2 + 2Ry + x^2 + y^2)^4} - \frac{1}{R^3} \right]
\end{aligned} \tag{27}$$

The closed-form solutions for the sensitivities make this problem another excellent choice for exploring the use of the complex variable sensitivity methods.

The diametrical compression test model was solved using three different meshes, with a coarse mesh consisting of 1148 elements and 2357 nodes; a moderately refined mesh of 2502 elements and 5093 nodes; and a fine mesh with 8,374 elements and 16,909 nodes. The solution for the stresses as calculated using the fine mesh appears in Figure 8. It should be noted that for each figure in this example, no solution is plotted for the elements that share the node where the load is applied. This is due to the fact that the stress on this node would be infinite.

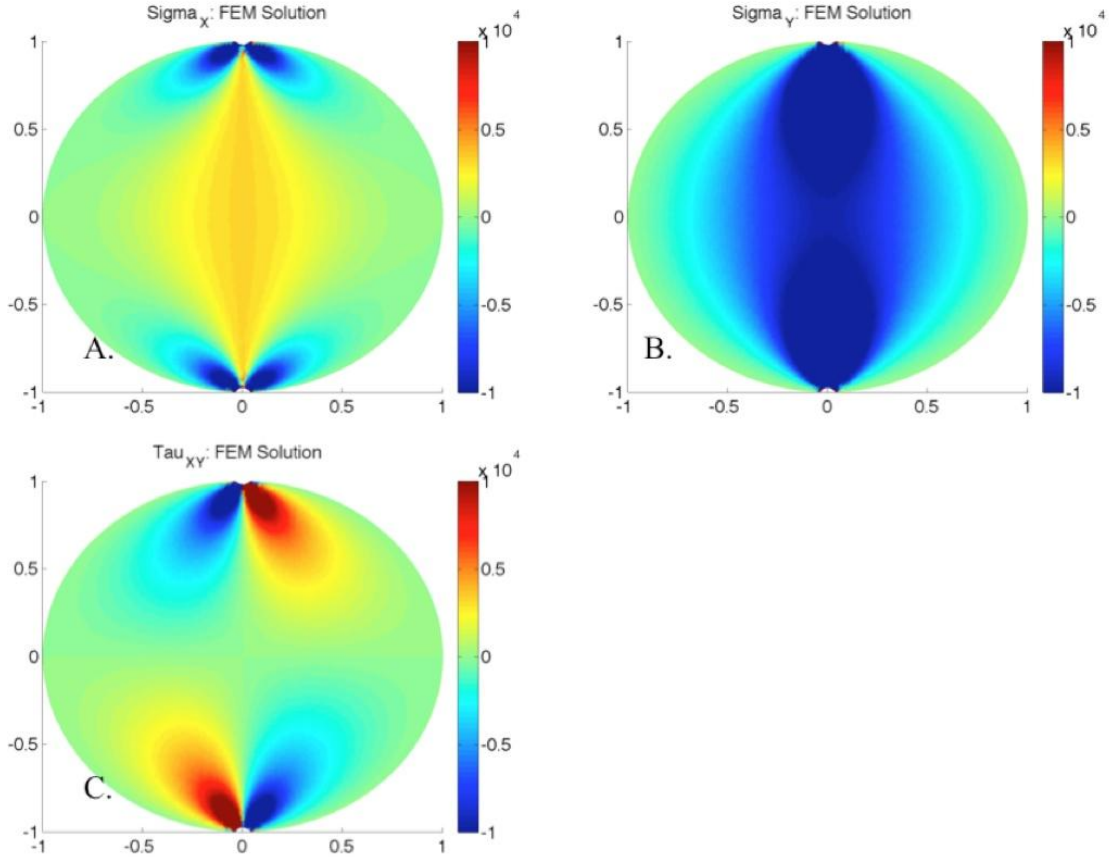


Figure 8. The Finite Element Solution for the Stresses in a Disc in Diametrical Compression. A) The Numerical Solution for the Stresses in the x-direction B) The Numerical Solution for the Stresses in the y-direction C) The Numerical Solution for the Shear Stress

The error norm used for this example is

$$error = \left| \frac{\sigma_{analytical} - \sigma_{numerical}}{\sigma_{analytical}} \right| \quad (28)$$

Table 7 shows the error for the three stresses for the three different mesh sizes using the error norm give in Equation 18. As before, it is seen that each successive mesh refinement results in a significant reduction in the error norm. This is shown visually in Figure 9. The red areas are regions of relatively higher error. As the number of elements increases, the total size of the red regions decreases significantly as the mesh is further refined. The computational time required to generate one solution for the three different mesh sizes is shown in Table 8.

Table 7. The Norm of the Error in the Stress Solutions for a Disk under Diametrical Compression

| Number of Elements | Norm of Error in Stress in X | Norm of Error in Stress in Y | Norm of Error in Shear Stress |
|--------------------|------------------------------|------------------------------|-------------------------------|
| 1148 | 1.261E-1 | 4.379E-2 | 9.717E-2 |
| 2502 | 8.633E-2 | 3.234E-2 | 6.122E-2 |
| 8374 | 4.578E-2 | 2.085E-2 | 3.953E-2 |

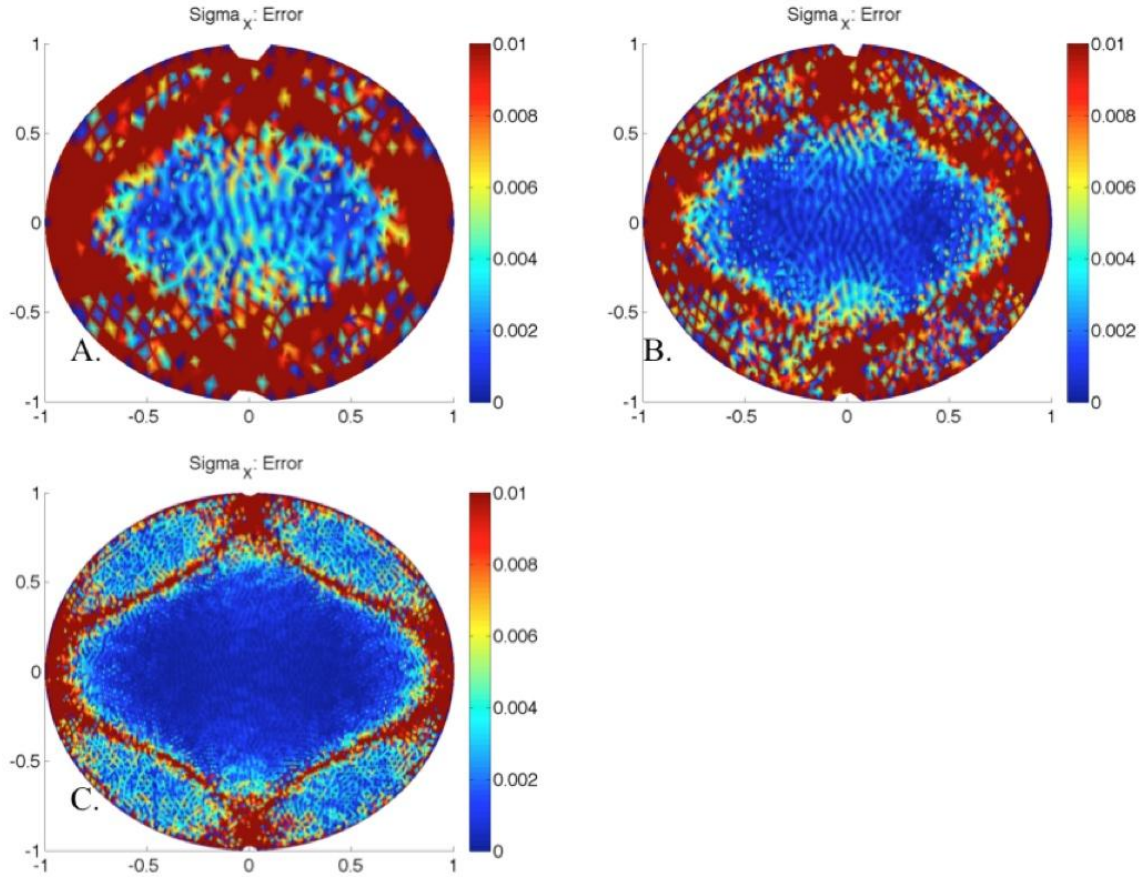


Figure 9. The Error in σ_x for Three Different Meshes for a Disk in Diametrical Compression. A) The error for the mesh with 1,148 elements and 2,357 nodes, B) The error for the mesh with 2,502 elements and 5,093 nodes, C) The error for the mesh with 8,374 elements and 16,909 nodes.

Table 8. The Computational Time Required to Solve each Model for a Disk under Diametrical Compression

| Number of Elements | Solution Time (s) |
|--------------------|-------------------|
| 1148 | 10.41 |
| 2502 | 27.82 |
| 8374 | 200.00 |

The errors in the sensitivities of the normal stress in the x-direction, calculated by each of the three methods are plotted in Figure 10 (first order) and Figure 11 (second order) for the fine mesh case. It is seen that there is again relatively higher error along the circumference of the disc due to boundary conditions. It is also noted that a few lines of relatively high error form inside the discs. These lines represent regions where the analytical sensitivity is zero or near zero. Since the analytical sensitivity appears in the denominator of the error formula given in Equation 28, the error becomes very large when the analytical sensitivity tends towards zero.

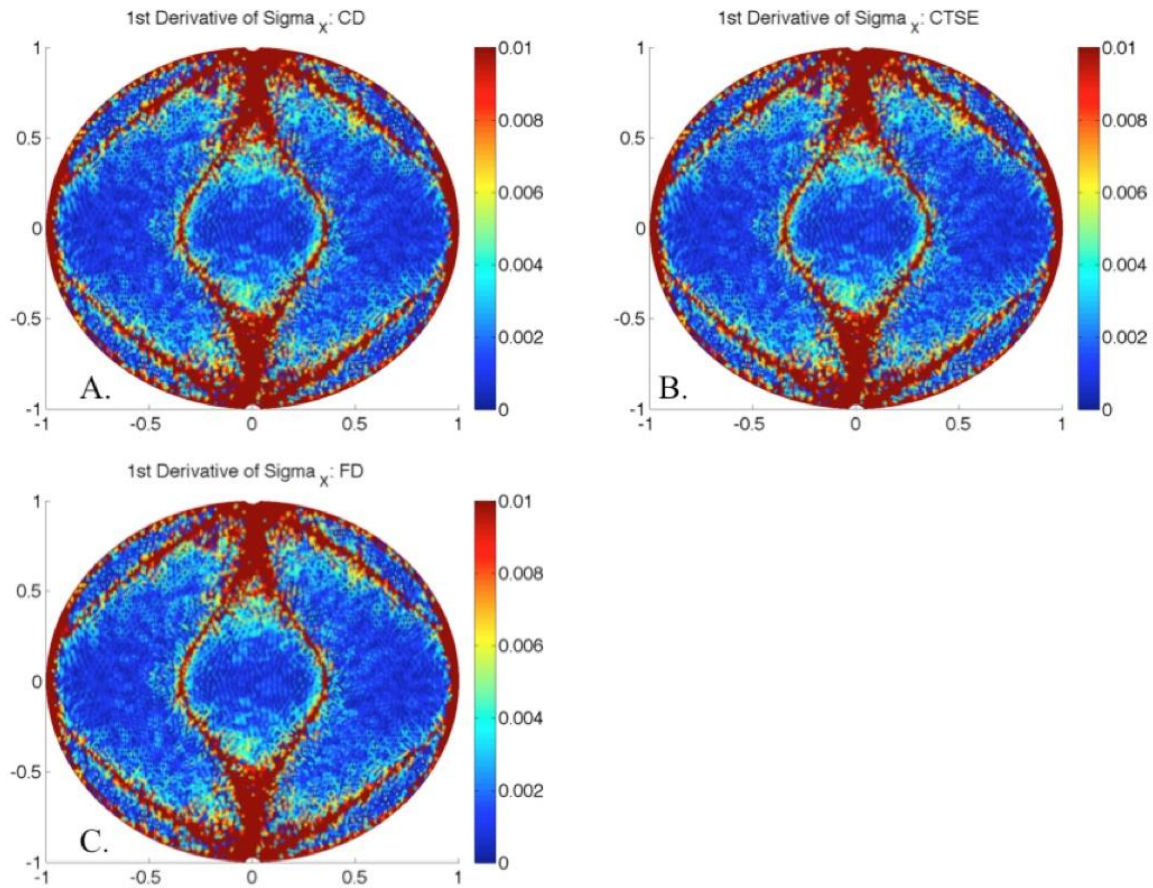


Figure 10. The Error in the First Order Sensitivity for a Disc in Diametrical Compression. A) Solution calculated by CD, B) Solution calculated by CTSE, C) Solution calculated by FD

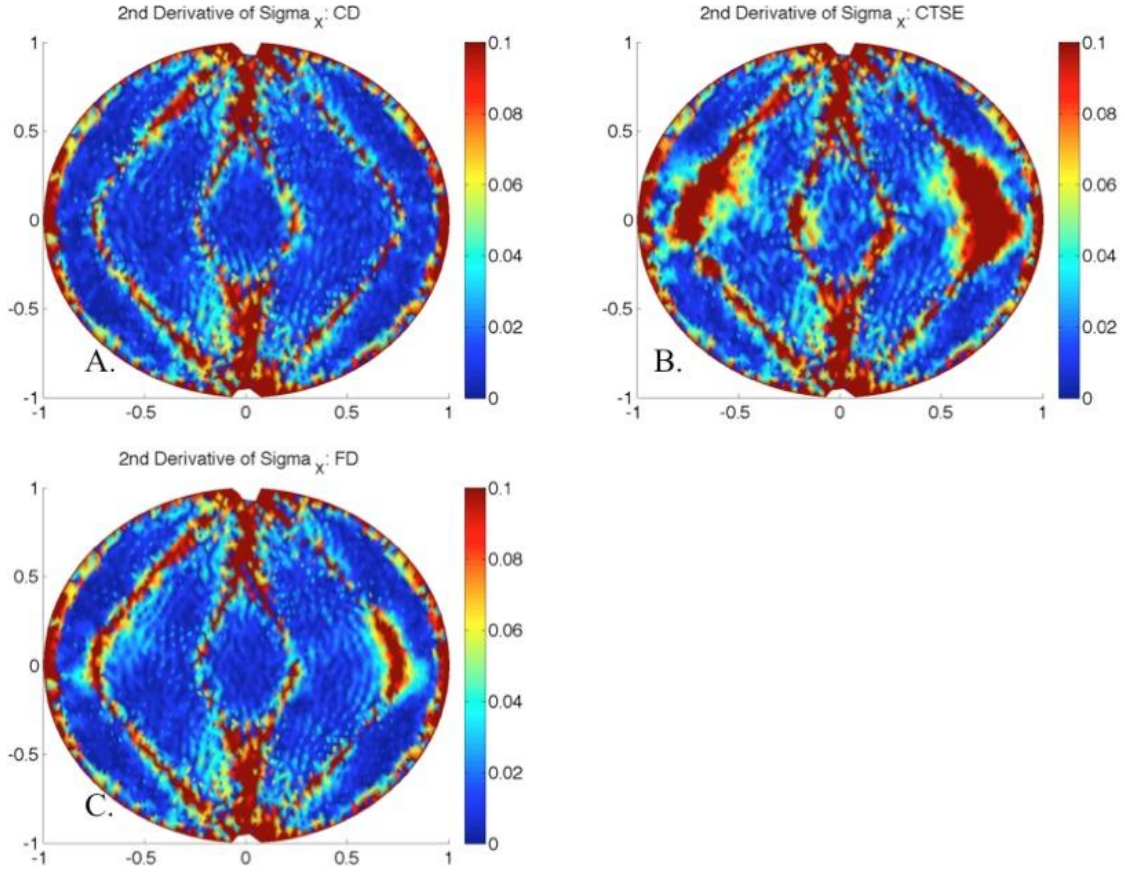


Figure 11. The Error in the Second Order Sensitivity for a Disc in Diametrical Compression. A) Solution calculated by CD, B) Solution calculated by CTSE, C) Solution calculated by FD

The norm of the error in the sensitivities is shown in Table 9. For this example, as compared to the thick walled cylinder, there is not a large dependence of the error norm on the number of elements. Also, there is not much difference between the methods themselves. This points to the fact that the error in the derivatives is not due to the truncation error of the derivative methods, since the truncation error of CTSE and CD should be of the order $O(h^2)$ while the truncation error of FD should be $O(h^6)$. The lack of dependence on the choice of method is further shown in Table 10 where the norm of the errors is shown for the 2502 element mesh for three different step sizes, or sampling radii. Very little variation in the error is seen as a function of the step size, which is not the behavior of truncation error.

Table 9. The Norm of the Error in the First Order Sensitivity of σ_x as a Function of the Number of Elements for a Disk under Diametrical Compression

| Number of Elements | CD | | CTSE | | FD | |
|--------------------|--------|--------|--------|--------|-----------------|--------|
| Order | 1st | 2nd | 1st | 2nd | 1 st | 2nd |
| 1148 | 0.4681 | 0.6378 | 0.4681 | 0.6379 | 0.4681 | 0.6378 |
| 2502 | 0.4164 | 0.5673 | 0.4164 | 0.5675 | 0.4164 | 0.5674 |
| 8374 | 0.4267 | 0.6572 | 0.4270 | 0.6581 | 0.4270 | 0.6577 |

Table 10. The Norm of the Error in the First and Second Order Sensitivities of the Radial Stress as a Function of Step Size for a Disk under Diametrical Compression

| Step Size | CD | | CTSE | | FD | |
|-----------|--------|--------|--------|--------|--------|--------|
| Order | 1st | 2nd | 1st | 2nd | 1st | 2nd |
| .0001 | 0.4164 | 0.5679 | 0.4164 | 0.5726 | 0.4164 | 0.5688 |
| .001 | 0.4164 | 0.5673 | 0.4164 | 0.5675 | 0.4164 | 0.5674 |
| .01 | 0.4143 | 0.5609 | 0.4166 | 0.5707 | 0.4164 | 0.5674 |

2.3.3 Numerical Example: Sensitivity of stress intensity factor with respect to crack length

In this example, CTSE was applied to several fracture mechanics problems to determine the sensitivity of the stress intensity factor with respect to crack length. Determining the stress intensity factor (K) at a crack tip and its sensitivity to changes in crack length (a) are important problems in fracture mechanics. A common method to calculate the stress intensity factor from finite element method results is to numerically compute a J -integral using the domain integral method and a truncated-pyramid virtual displacement (Q) function. As shown below, the first order derivative of the J integral (or K) with respect to crack length can be determined using CTSE by adding an imaginary step (h) to the elements' nodal coordinates and applying Equation 17. This methodology achieves high accuracy over a wide range of imaginary step sizes for the two-dimensional (2D) problems tested to date.

Four well-known two-dimensional fracture mechanics problems, the single- and double-edge crack, central crack, and an infinite array of collinear cracks, can all be modeled using the same geometry, material properties, and remote loading, by varying the boundary conditions along symmetry planes as shown in Figure 12.

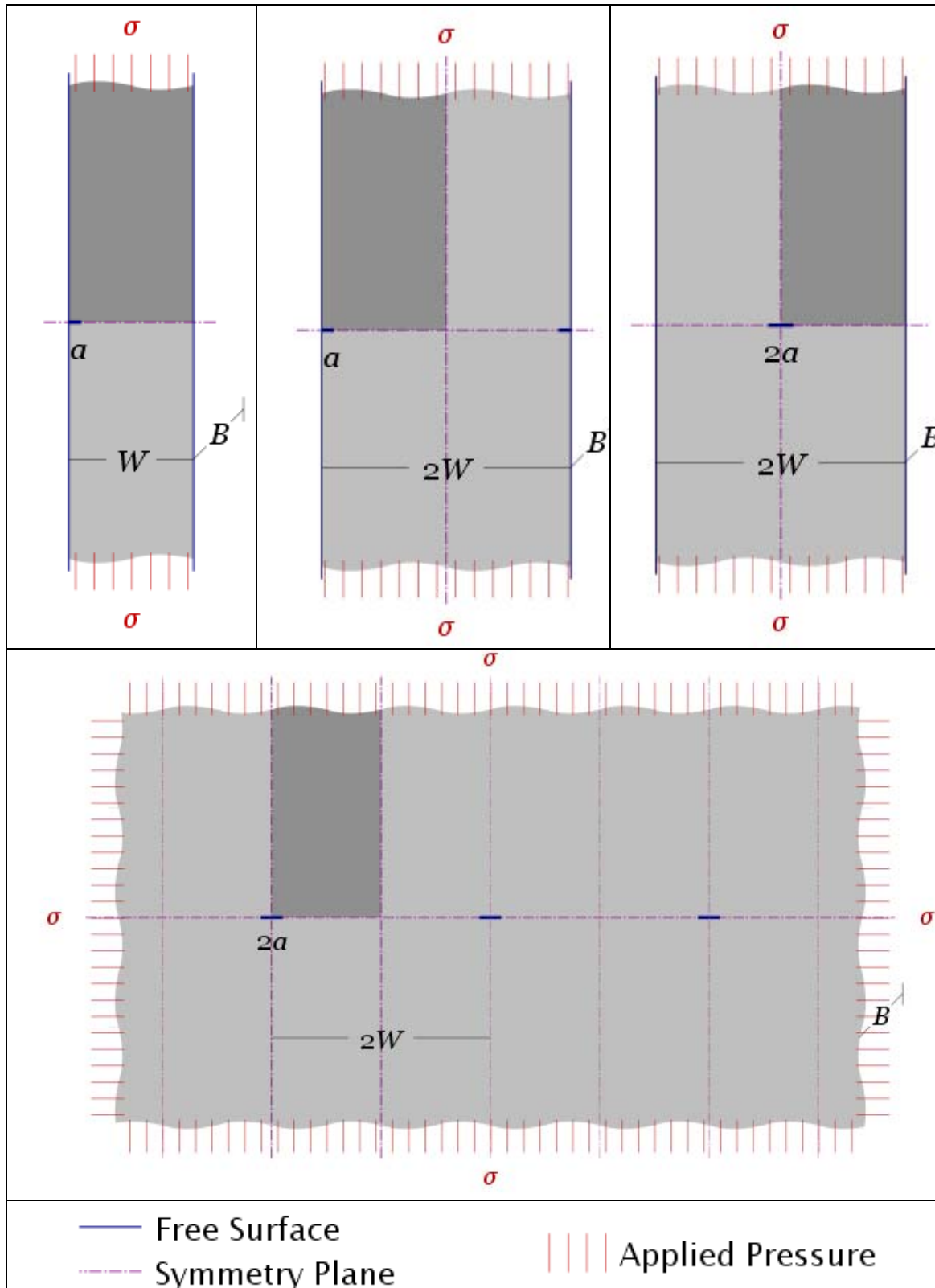


Figure 12. The Four Problems Modeled for Example 3, A) Single Edge Crack (SENT), B) Double Edge Crack (DENT), C) Center Crack (CCT), D) Infinite Array of Collinear Cracks. The darker shaded area indicates the common geometry.

The mode I reference solutions for these problems are shown in Table 11. The infinite array of collinear cracks is particularly attractive as it has closed-form solution for K . The other K solutions are approximate fits to the numerical solutions.

Table 11 Reference Formulas for the Stress Intensity Factor (K)

| Geometry | $K_{I,ref} = \sigma_{remote} \sqrt{aY}$ |
|--|---|
| Single Edge Crack^[30] (SENT) | $\sigma_{remote} \sqrt{\pi a} \frac{\sqrt{2 \tan \frac{\pi a}{2W}}}{\cos \frac{\pi a}{2W}} \left(0.752 + 2.02 \frac{a}{W} + 0.37 \left(1 - \sin \frac{\pi a}{2W} \right)^3 \right)$ |
| Double Edge Crack^[31] (DENT) | $\sigma_{remote} \sqrt{\pi a} \sqrt{\frac{W}{\pi a} \left(\tan \frac{\pi a}{W} + 0.1 \sin \frac{2\pi a}{W} \right)}$ |
| Central Crack^[32] (CCT) | $\sigma_{remote} \sqrt{\pi a} \sqrt{\sec \frac{\pi a}{2W} \left(1 - 0.025 \left(\frac{a}{W} \right)^2 + 0.06 \left(\frac{a}{W} \right)^4 \right)}$ |
| Infinite Array^[33] | $\sigma_{remote} \sqrt{\pi a} \sqrt{\frac{2W}{\pi a} \tan \frac{\pi a}{2W}}$ |

All of these problems assume an infinite longitudinal length (L), i.e., the height in **Figure 12**, but a model with a finite geometry produces a good approximation of the stress fields when the crack length is much less than height of the model.

The sensitivities of K to crack length can be found by differentiating these formulas with respect to a as shown in Table 12.

Table 12 The First Partial Derivative of Each Reference Formula with Respect to Crack Length

| | |
|---------------------------------|---|
| | $K' = \partial K_{I,ref} / \partial a$ |
| Single Edge Crack (SENT) | <i>Too lengthy to be included here</i> |
| Double Edge Crack (DENT) | $\frac{\sqrt{10}}{10} \pi \sigma_{remote} \frac{\cos \frac{2\pi a}{W} + 5 \sec^2 \frac{\pi a}{W}}{\sqrt{W \left(\sin \frac{2\pi a}{W} + 10 \tan \frac{\pi a}{W} \right)}}$ |
| Central Crack (CCT) | $\frac{\sigma_{remote}}{800W^5} \sqrt{\frac{\pi}{a} \sec \frac{\pi a}{2W}} \left(400W^5 + 200\pi W^4 a \tan \frac{\pi a}{2W} - 50W^3 a^2 - 5\pi W^2 a^3 \tan \frac{\pi a}{2W} + 216Wa^4 + 12\pi a^5 \tan \frac{\pi a}{2W} \right)$ |
| Infinite Array | $\frac{\sqrt{2}}{4} \pi \sigma_{remote} \frac{\sec^2 \frac{\pi a}{2W}}{\sqrt{W \tan \frac{\pi a}{2W}}}$ |

In these problems, the stresses around the crack tip are pure mode I so the stress intensity factor may be determined from the J -integral values calculated using the finite element results as $K_I = \sqrt{JE'}$ where $E' = E$ for plane stress and $E' = E/(1 - \nu^2)$ for plane strain.

These four related problems use the same finite element mesh of eight-noded bi-quadratic quadrilaterals with degenerate quarter-point nodes around the crack tip. The material properties and loading conditions are also the same and the problems differ only in the boundary conditions applied. The numerical values used for the problems are shown in Table 13.

Table 13 Parameters of the Plane Strain Problems Investigated

| | | |
|-----------------|-------------------|-------------------|
| Remote Load | σ_{remote} | 100×10^3 |
| Elasticity | E | 10×10^9 |
| Poisson's Ratio | Y | 0.3 |
| Height | L | 2 |
| Thickness | B | 1 |
| Width | W | 1 |
| Crack Length | A | 0.100 |

In order to determine the derivative of K with respect to crack size, a complex variable finite code (CFEM) was written for 2D linear elasticity analysis with a J integral domain integration

calculation. The J integral results from CFEM were verified against results from Abaqus using identical finite element meshes.

The recommended mesh to use around a crack tip in order to obtain accurate J integral calculations is called a “spider web mesh” of which a schematic is shown below. The mesh consists of a number of concentric rings of elements around the crack tip. The mesh in Figure 13 consists of 6 concentric rings of elements. The heavy black line with gray interior indicates that the J integral was computed using this integration domain, i.e., 5 rings of elements. The elements in ring 1 are collapsed quadrilaterals elements with quarter point locations for mid-side nodes. The parameters used in the following numerical examples are given in Table 14.

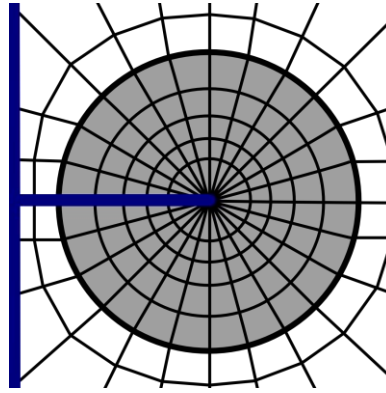


Figure 13 Schematic of "Spider Web" Finite Element Mesh Used for J Integral Calculations

Table 14 Selected Finite Element Model Characteristics

| | |
|------------------------------------|----------------------|
| Approximate Domain Q_1 Radius | 1.5×10^{-6} |
| Largest Domain (Q_{36}) Radius | $0.75a$ |
| Radial Elements | 36 |
| Circumferential Elements | 36 |
| Number of Elements | 12,482 |
| Number of Nodes | 37,957 |
| Degrees of Freedom | 75,914 |

Although complex number operations typically require three times the computational effort of their real-valued equivalent, for many problems only a limited number of scalar values have an imaginary step applied. When estimating shape sensitivities, the number of complex operations needed is approximately proportional to the fraction of the node ordinates affected by the imaginary displacement, so that the total computational effort is less than it would be if all operations needed to be complex. Typical timing estimates are shown in Table 15.

Table 15 Typical Computation Times. *Note These Values Should Not Be Compared To Those In Table 4 Since This Example Uses A Different CFEM Implementation*

| Imaginary Displacement Meethod | Time to Build Stiffness Matrix (s) | Time to Solve for System Displacement (s) | Time to Calculate J for all Integration Domains (s) | Total Solution Time (s) |
|---------------------------------------|---|--|---|--------------------------------|
| None (Pure Real) | 27.9 | 2.4 | 1.6 | 31.9 |
| Tip Node | 28.0 | 4.9 | 1.7 | 34.6 |
| Domain 1 | 28.0 | 4.9 | 1.6 | 34.5 |
| Crack Face | 28.0 | 4.9 | 1.6 | 34.5 |
| Domain 4 | 28.0 | 4.9 | 1.8 | 34.7 |

When a 2D finite element mesh represents a solid body with a straight crack, there are many ways to perturb the nodes to increase the crack length by a small imaginary amount ih . One simple method is to move only the node at the crack tip a small amount in the direction of crack extension. Another method is to move all the nodes along the crack face in the direction of crack extension proportional to the distance from the crack mouth so that the tip node moves ih and the nodes at the mouth remain unperturbed. These methods have the disadvantage of changing the relative locations of some of the effected elements' mid-side nodes, i.e., the mid-side nodes on the crack face, so they are no longer precisely at mid- or quarter-points, and therefore represent a change in both crack length and a change to the elements' shape functions, resulting in less accurate results. Although the effect is not large, it does affect the accuracy of the computed derivative of the J integral. A schematic of this effect is shown below.

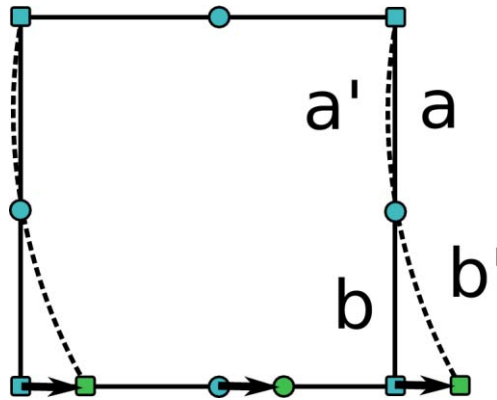


Figure 14 Schematic of the Effect of Perturbing only the Nodes Along the Crack Face

A solution to this problem is to perturb all the elements within a user-defined group around the crack tip as a rigid body in the imaginary domain. For example, in Figure 15, all the nodes along the black line (ring 5) remain unperturbed, whereas, the nodes within ring 4 are all perturbed as a rigid body. In this case, we call the perturbation method Q_4 to indicate the all the nodes within ring 4 are perturbed as a rigid body. Obviously, any ring can be chosen for the perturbation. As shown in figures below, the highest accuracy appears to be obtained when using Q_4 for the imaginary perturbation, then using the J integral results obtained from a ring of elements larger than Q_4 .

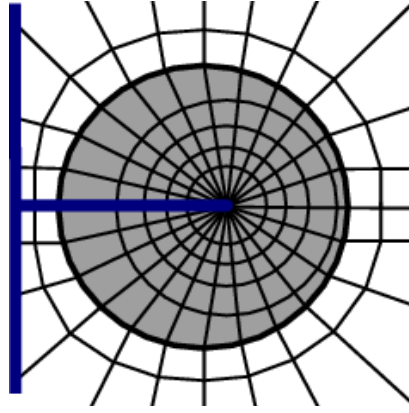


Figure 15 Schematic of Rigid Body Perturbation of Nodes Around the Crack Tip

Since the effect of the complex step h is relative to the size of the elements having their nodes perturbed, the complex step h is normalized by h_1 , with h_1 defined as the smallest real-valued distance by which any corner node can be moved in the displacement direction without overtaking another node.

Table 16 compares the mode I stress intensity factor and the stress intensity factor derivative results for the infinite array problem from CFEM using the J integral (K_{CFEM}), computed using the J integral with Abaqus (K_{Abq}), from the reference solution (K_{ref}), and the first order derivatives obtained using CTSE within CFEM (K'_{CFEM}) and the solution in Table 12 (K'_{ref}). Four different methods were used to implement the perturbation of the crack length in the imaginary domain. The results reported are obtained from the 36th ring of circumferential elements.

Table 16 Accuracy of K and K' for Four Methods of Imaginary Displacement for the Infinite Array Problem, J-Integration Domain 36, $h/h_1 = 10^{-6}$

| | K_{CFEM}/K_{Abq} | K_{CFEM}/K_{ref} | K'_{CFEM}/K'_{ref} |
|--------------------------|--------------------|--------------------|----------------------|
| Single Edge Crack | | | |
| Tip Node | 0.983060 | 0.977694 | 0.990846 |
| Domain 1 | 0.983060 | 0.977694 | 0.990833 |
| Crack Face | 0.983060 | 0.977694 | 0.991554 |
| Domain 4 | 0.983060 | 0.977694 | 0.989891 |
| Double Edge Crack | | | |
| Tip Node | 0.999718 | 1.010374 | 0.962984 |
| Domain 1 | 0.999718 | 1.010374 | 0.962971 |
| Crack Face | 0.999718 | 1.010374 | 0.963675 |
| Domain 4 | 0.999718 | 1.010374 | 0.962056 |
| Central Crack | | | |
| Tip Node | 0.999510 | 0.999613 | 1.001053 |
| Domain 1 | 0.999510 | 0.999613 | 1.001039 |
| Crack Face | 0.999510 | 0.999613 | 1.001776 |
| Domain 4 | 0.999510 | 0.999613 | 1.000088 |
| Infinite Array | | | |
| Tip Node | 0.999591 | 0.999623 | 1.000761 |
| Domain 1 | 0.999591 | 0.999623 | 1.000748 |
| Crack Face | 0.999591 | 0.999623 | 1.001485 |
| Domain 4 | 0.999591 | 0.999623 | 0.999797 |

Figure 16 shows the results for K as a function of the J integration domain. The results indicate that the most accurate solution is obtained from the J integral domain 4, e.g., 4th ring of elements. This result appears to be independent of the complex perturbation method.

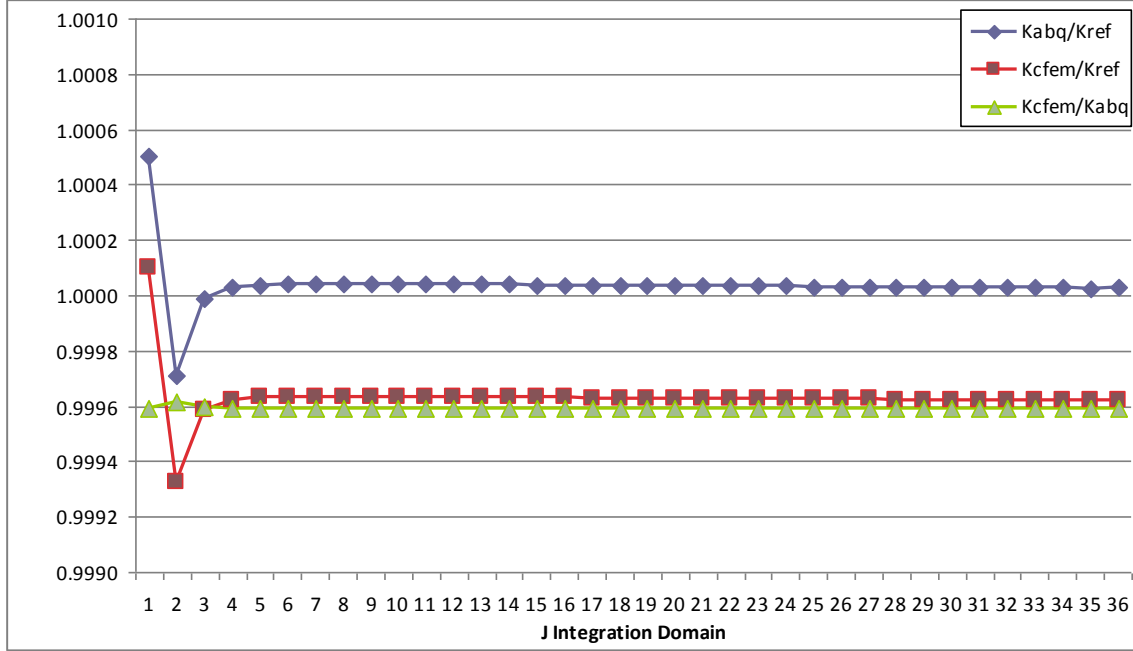


Figure 16. CFEM and ABAQUS Infinite Array Stress Intensity Factor (K) Accuracy vs. J integral domain

The results in Table 16 and Figure 16 indicate close agreement in K between CFEM and Abaqus, independent of the implementation of the complex perturbation of the crack length; the stress intensity factors calculated by CFEM and Abaqus are both within the expected errors of the reference formulas and solution methods used. As described in Section 2.2.1, the imaginary step size has an effect on the real-valued solution of $O(h^2)$, but if h is sufficiently small, the J integral calculation will not be significantly effected as shown in this analysis.

Figure 17 shows the accuracy in K'_{CFEM}/K'_{ref} as a function of the J integration domain for the 4 different perturbation methods. Figure 18 shows a closer view of the same data. These data indicate from which domain the J' integral should be extracted as a function of the perturbation method. From Figure 17, the results from the Tip Node, Domain 1, and Domain 4 methods all converge at around the 4th integration domain. The results for the Face Only method don't converge until about the 24th integration domain. The close up view in Figure 18 indicates that ultimately, the best results are obtained from the 36th domain using the Q_4 method to implement the imaginary crack length perturbation.

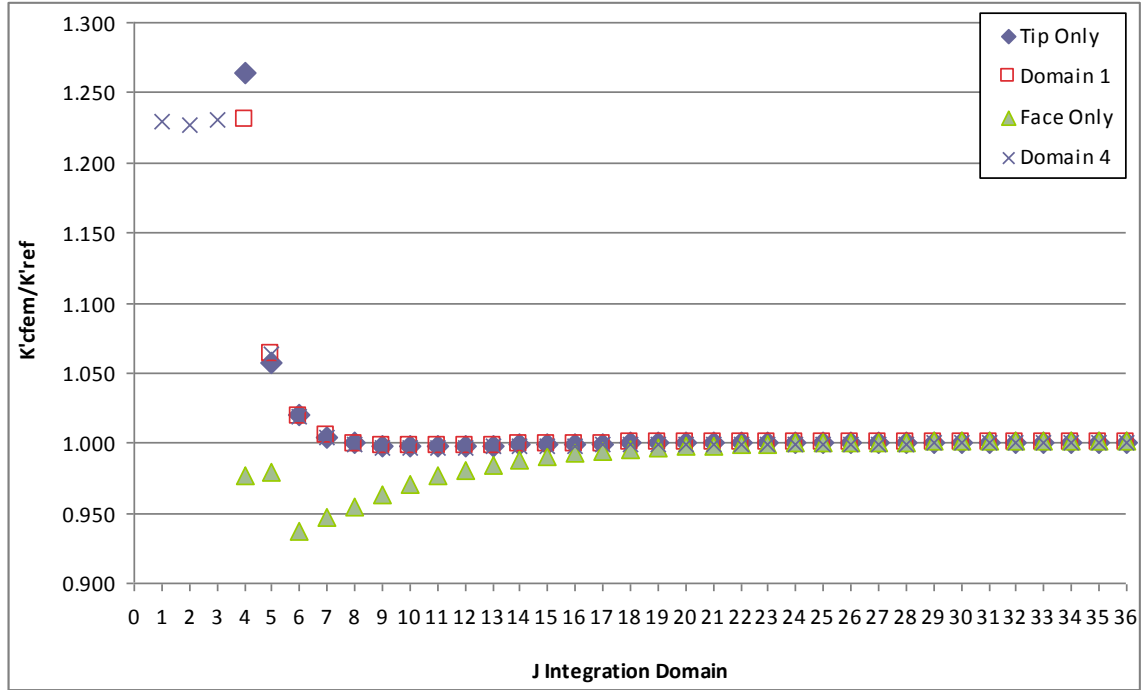


Figure 17. Imaginary Displacement Method Influence on K' Accuracy, Infinite Array, $h/h_1 = 10^{-6}$, CFEM K' within 30% of Reference

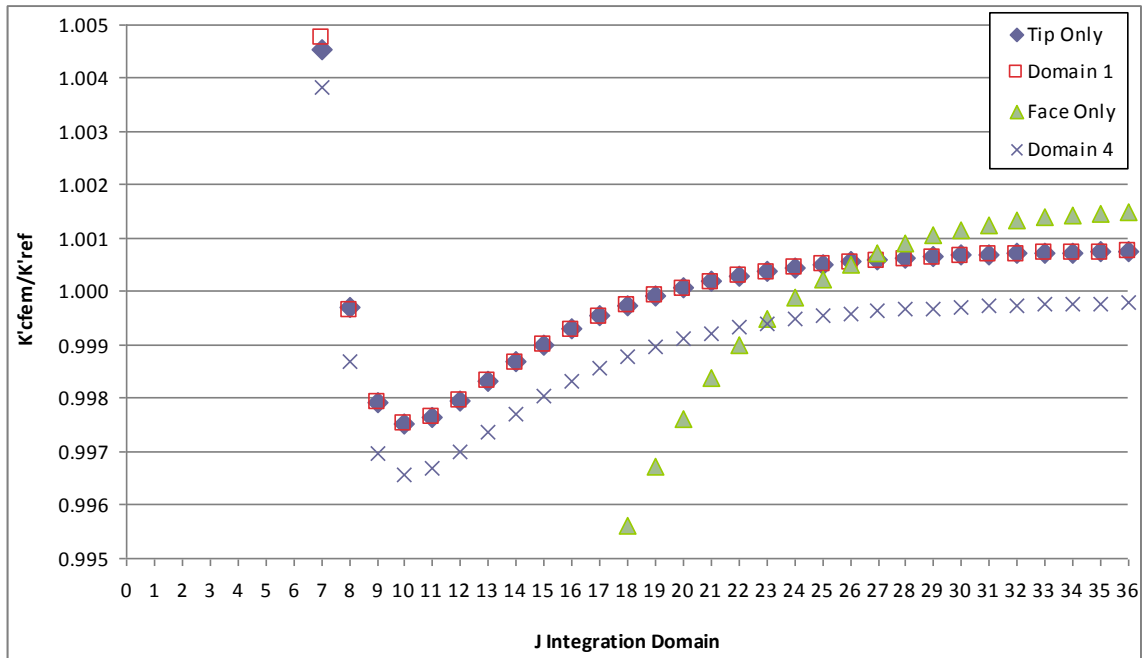


Figure 18. Imaginary Displacement Method Influence on K' Accuracy, Infinite Array, $h/h_1 = 10^{-6}$, CFEM K' within 0.5% of Reference

These results suggest that using CTSE to estimate the first-order sensitivity of K with respect to a change in a is more accurate when larger integration domains are used to calculate K . Because of this, the largest J -integration domain (36) is used to examine the effects of varying the CTSE

complex step size h on the the accuracy of K and K' in Figure 19. The results show the remarkable stability of the method since h/h_1 varies from 10^{-1} to 10^{-300} .

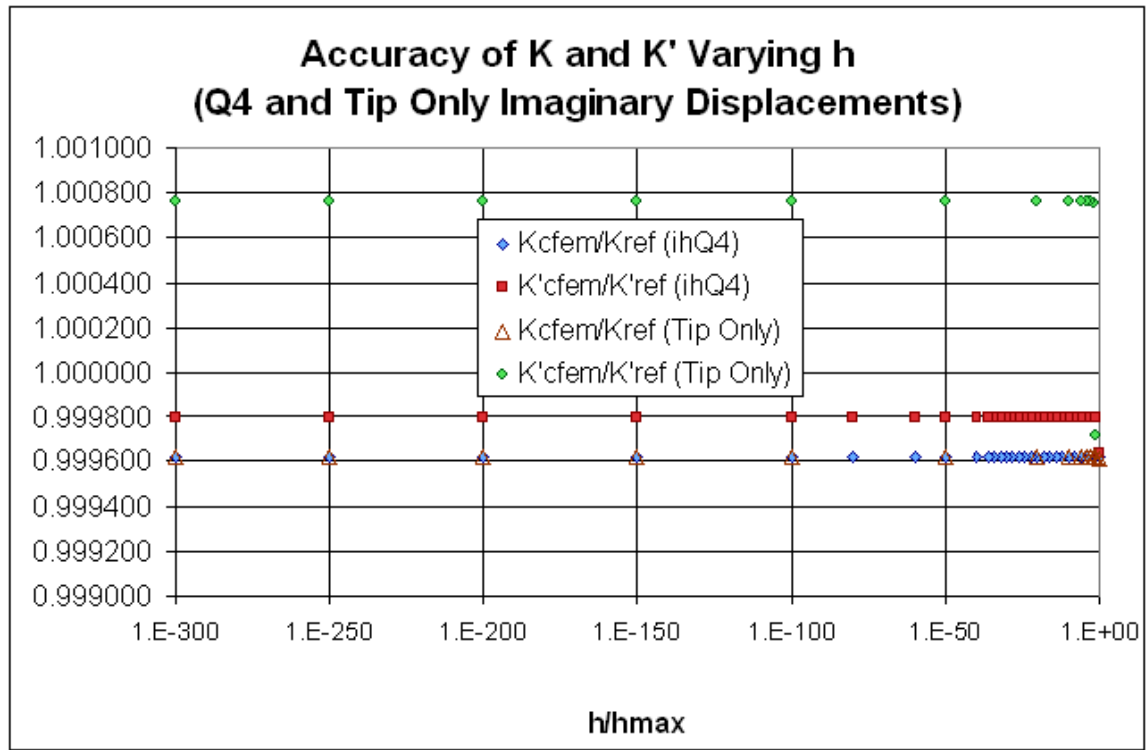


Figure 19 Accuracy of K and K' over a wide range of Complex Step Size

3 Probabilistic Sensitivity Analysis with respect to Bounds of Truncated Distributions

The Score Function (SF) method is a mathematical technique to compute the partial derivative of the probability-of-failure, mean (μ_Z) or standard deviation (σ_Z) of some response (Z) with respect to the parameters of the input PDFs, e.g. (μ_i, σ_i) [34]. Under this program, the SF method was extended to address the case of computing the probabilistic sensitivities with respect to bounds of truncated distributions. Examples of truncated distributions include uniform, truncated normal, and truncated Weibull among others.

Bounds on variables are often implemented as part of a quality control program to ensure a sufficient pedigree of a product component and these bounds may significantly affect the product's reliability and design through constraints such as cost, manufacturability and reliability. The methodology to compute the sensitivity of the probability-of-failure with respect to bounds of truncated distributions is summarized below. Extension to the sensitivities of the mean and standard deviation of the response can be found in ref. [35]

3.1 Methodology

The probability-of-failure integral can be written

$$P_f = \int_{-\infty}^{\infty} I(\mathbf{x}) f_{\mathbf{x}}(\mathbf{x}) d\mathbf{x} \quad (29)$$

where \mathbf{x} represents a vector of random variables, $I(\mathbf{x})$ denotes the indicator function, (1 if failure occurs, 0 otherwise), and $f_{\mathbf{x}}$ represents the joint probability density function of the random variables.

The derivative of the probability integral with respect to a parameter of a random variable that affects the boundary can be determined by using the idea of the classical Material Derivative from continuum mechanics [36],

$$\frac{D}{Dt} \int_V \Psi(\mathbf{x}, t) dV = \int_V \frac{\partial \Psi(\mathbf{x}, t)}{\partial t} dV + \int_S \Psi(\mathbf{x}, t) \mathbf{v}_j \mathbf{n}_j dS \quad (30)$$

where Ψ is a property of the continuum, \mathbf{v} denotes the velocity of the material, \mathbf{n} represents the unit normal along the boundary S , and V is the volume enclosed by S . The surface integral term in Equation 30 is the value of Ψ on the boundary multiplied by the volume swept by the particles on the boundary in the time interval dt , integrated over dS . This term can be considered as a flux of the property Ψ over the surface S .

The concept of the material derivative can be utilized to take the derivative of the probability integral, Equation 30, with respect to a bound of a random variable PDF. Here, the independent parameter, θ_i , is a bound of the distribution representing X_i , the JPDF is equivalent to the property Ψ , the volume is the N dimensional random variable space, and S is the surface of the random variable space remaining when random variable X_i is set to the bound θ_i . For rectangular truncation, the surface S is straightforward to compute as the independent parameter, θ_i , is a bound of the N dimensional random variable space.

The unit normal and the equivalent velocity term and their relation can be discerned from a problem of two random variables, see Figure 20. Since the independent parameter θ is an element of \mathbf{X} , the velocity becomes $v = \partial x / \partial \theta = 1$. At the lower bound v and n are in opposite directions, hence, the dot product $v_j n_j$ equals -1. At the upper bound $v_j n_j$ equals +1.

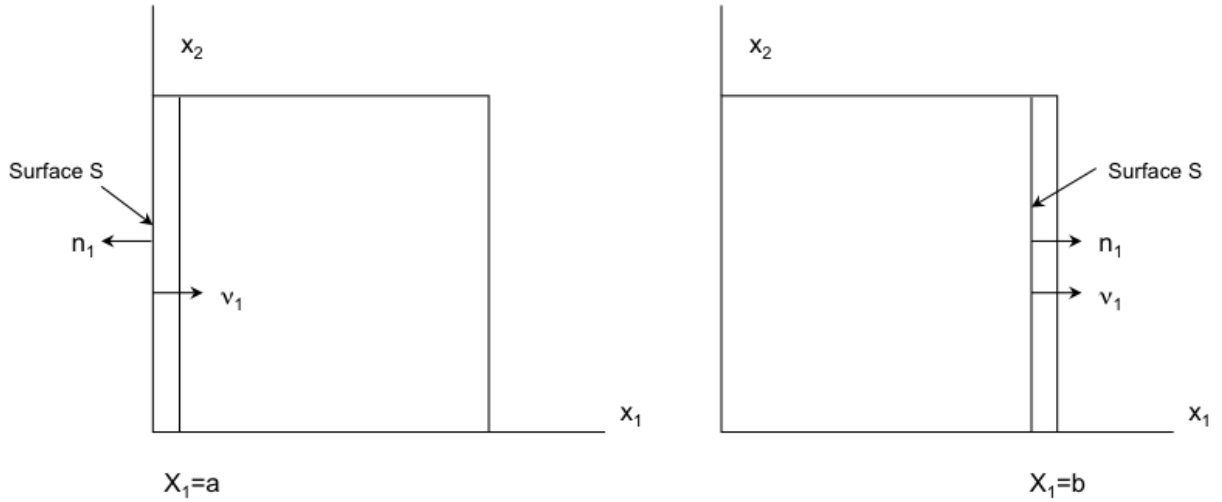


Figure 20 Descriptions of Velocity and Unit Normal Along Bounds

Carrying out the Material Derivative of the probability-of-failure integral, the sensitivities become

$$\frac{\partial P_f}{\partial a_i} = f_{X_i}(a)(P_f - P_I^a) \quad (31)$$

$$\frac{\partial P_f}{\partial b_i} = -f_{X_i}(b)(P_f - P_I^b) \quad (32)$$

where P_f represents the usual probability-of-failure integral and P_I^a and P_I^b denote supplemental flux integrals. Thus, the effort to obtain the sensitivities becomes one of evaluating the flux integrals P_I^a and P_I^b in addition to the probability-of-failure.

The flux integral can be evaluated by integrating the joint probability density function times the indicator function over the surface S defined by the condition $x_i = \theta$. That is, one integrates the JPDF in the failure region over the surface S . Thus, the dimension of the flux integral is $N-1$. A schematic of the flux in two dimensions (two random variable problem) is shown in Figure 21 where the value of the joint PDF along the upper bound of X_1 is outlined.

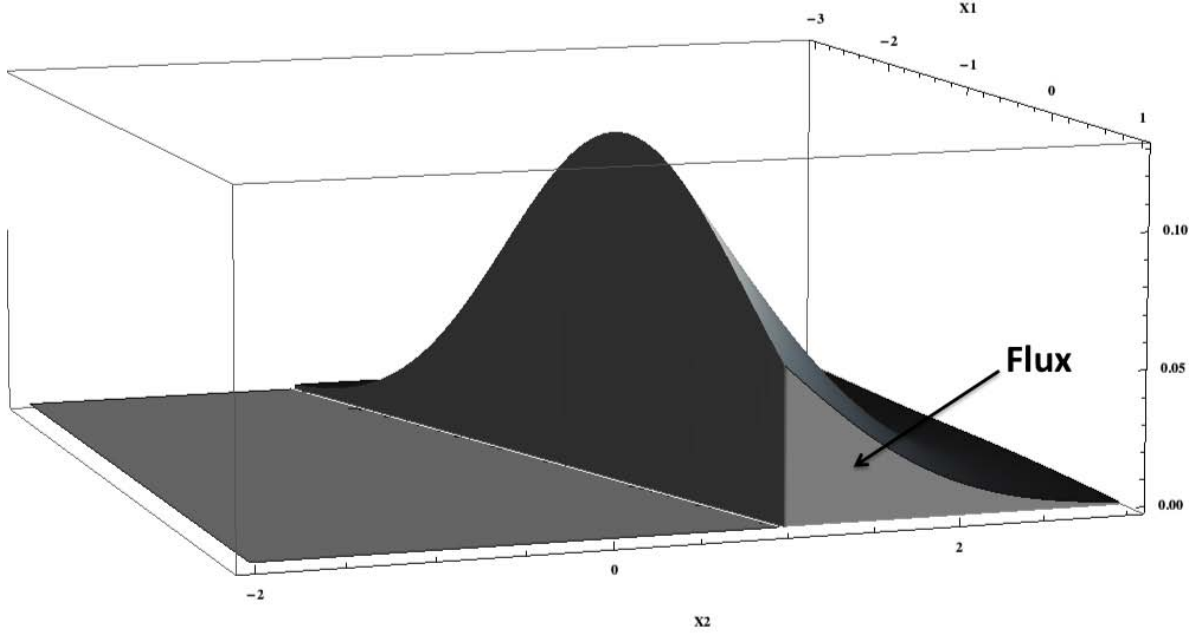


Figure 21 Flux of the JPDF in the Failure Region over the Surface S

It is straightforward to calculate the flux integrals using sampling as

$$P_I^\theta \approx \frac{1}{m} \sum_{k=1}^m I(\mathbf{y}_k, \theta) \quad (33)$$

That is, the samples used to compute P_f are reused to compute P_I^θ by projecting the samples onto the surface $X_i = a$ or $X_i = b$ and the indicator function is evaluated along the surface $X_i = \theta_i$.

3.2 Results and Discussion

3.2.1 Numerical Example

A two dimensional example is solved to illustrate the concepts. Consider a limit state of $g(r,s) = r - s$ with R and S modeled as independent random variables. The indicator function defines the failure region as

$$I[r,s] = \begin{cases} 1 & \text{if } g(r,s) \leq 0 \\ 0 & \text{otherwise} \end{cases} \quad (34)$$

R is a standard normal distribution and S is a uniform distribution with bounds $a = 0$ and $b = 1$.

$$f_R(r) = \frac{1}{\sqrt{2\pi}} \text{Exp}[-r^2/2] \quad -\infty \leq r \leq \infty \quad (35)$$

$$f_S(s) = \begin{cases} 1 & 0 \leq s \leq 1 \\ 0 & \text{otherwise} \end{cases} \quad (36)$$

Table 17 summarizes results obtained using both the flux-based methodology and the standard finite difference (forward differencing) method. The derivatives of the probability-of-failure with respect to the bounds were computed using Eqs. (31) and (32) using both symbolic integration and sampling. Finite difference estimates were also computing using symbolic integration and sampling with a forward step size of 0.00001.

Table 17 Probabilistic Sensitivity Results for Limit State $g = r - s$ (R Standard Normal, S Uniform)

| | Flux-based | | Finite Difference | |
|---|------------------------|-------------------------------|------------------------|-------------------------------|
| | Integration (exact) | Sampling (10^4 samples) | Integration (exact) | Sampling (10^6 samples) |
| $\frac{\partial \mathcal{P}_f}{\partial a}$ | 0.1844 | 0.1842 ¹ | 0.1844 | .1876 ¹ |
| $\frac{\partial \mathcal{P}_f}{\partial b}$ | 0.1560 | 0.1571 ¹ | 0.1570 | .1608 ¹ |

¹expected value of 100 trials

The sensitivities for the flux-based and finite difference methods using exact integration are very close, as expected. The results using sampling are also in good agreement; however, note that 10^4 samples were used for the flux-based approach to obtain a solution with good accuracy versus 10^6 samples for the finite difference sampling-based approach. The superiority of the flux-based approach compared to the standard finite difference (forward differencing) approach using sampling can be shown clearly by comparing the 95% confidence bounds and the coefficient of variation (COV = standard deviation/mean) obtained using both methods obtained from 100 trials. Figure 22 shows a plot of the 95% confidence bounds for finite difference (dashed) versus flux-based (solid) for $\partial \mathcal{P}_f / \partial a$ (similar results are obtained for $\partial \mathcal{P}_f / \partial b$). The number of samples

are shown in the X axis in \log_{10} scale. The bounds for the flux-based approach are so much narrower than the finite difference approach that they show almost as a straight line. The bounds are so wide for the finite difference method that any solution obtained is completely unreliable until the number of samples approaches one million.

A closer examination of the benefits of using common random variables during the sampling process is provided in Table 18. Variance results for negative, approximately zero, and positive sampling correlation are provided. The results clearly show that positive correlation provides approximately a three times reduction in the variance of the sensitivities with respect to independent sampling; at zero cost. Positive correlation was accomplished simply by using the same samples to compute the probability-of-failure and the fluxes.

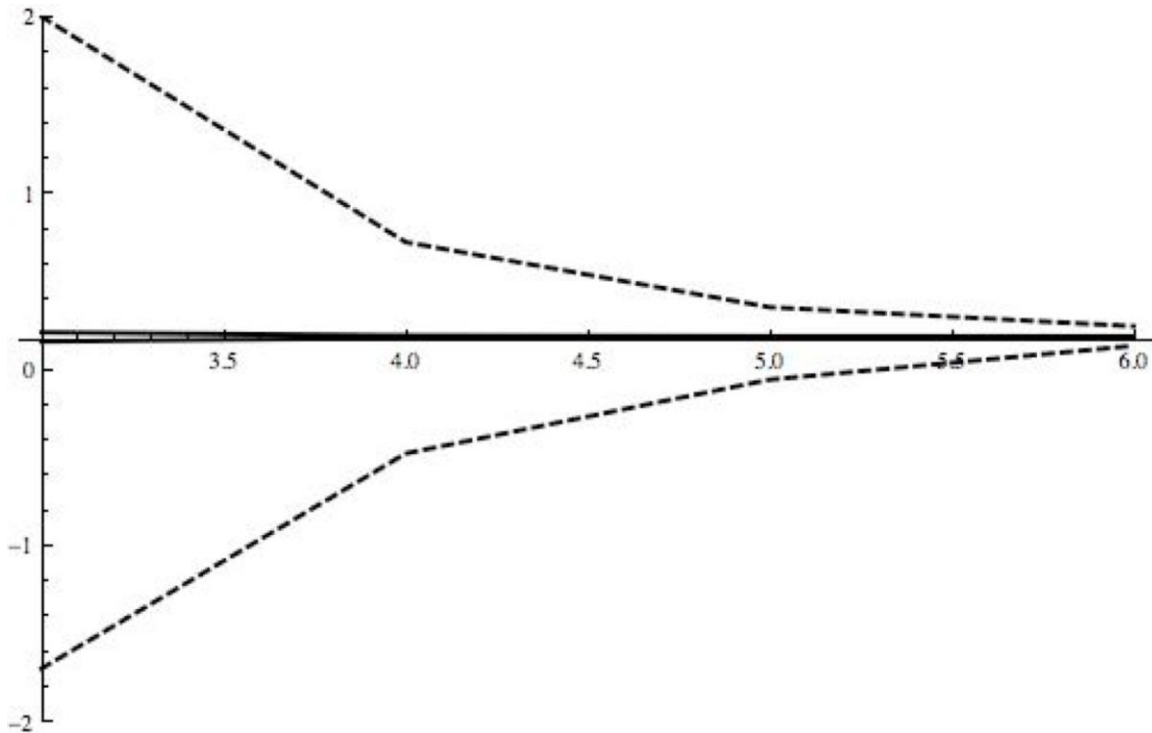


Figure 22 95% confidence limits (100 trials) for $\partial P_f / \partial a$ as a function of the number of samples in \log_{10} scale (dashed - finite difference; solid – flux based)

Table 18 Variance of sensitivity estimates $\partial P_f / \partial \theta$ as a function of sampling correlation (100 trials) – actual correlation in parentheses

| # Samples | $\frac{\partial P_f}{\partial a}$ ($\rho < 0$) | $\frac{\partial P_f}{\partial a}$ ($\rho \approx 0$) | $\frac{\partial P_f}{\partial a}$ ($\rho > 0$) | $\frac{\partial P_f}{\partial b}$ ($\rho < 0$) | $\frac{\partial P_f}{\partial b}$ ($\rho \approx 0$) | $\frac{\partial P_f}{\partial b}$ ($\rho > 0$) |
|--------------|---|---|---|---|---|---|
| 10^3 | 8.81E-4 ($\rho = -0.75$) | 4.64E-4 ($\rho \sim 0$) | 1.37E-4 ($\rho = 0.82$) | 4.84E-4 ($\rho = -0.46$) | 3.48E-4 ($\rho \sim 0$) | 1.29E-4 ($\rho = 0.78$) |
| 10^4 | 7.37E-4 ($\rho = -0.66$) | 4.01E-5 ($\rho = 0.09$) | 1.44E-5 ($\rho = 0.68$) | 4.03E-4 ($\rho = -0.27$) | 2.70E-5 ($\rho = 0.09$) | 1.22E-5 ($\rho = 0.64$) |

Table 19 shows the coefficient of variation of the two methods as a function of the number of samples. The COV for the finite difference method is approximately two orders of magnitude larger than that obtained using the flux-based method for the same number of samples. These results imply that there are approximately 4 orders of magnitude difference in the number of samples required to achieve similar accuracy using both methods. The explanation is that the finite difference method requires an approximation of a limiting process estimated by subtracting two near-equal numbers. The flux-based approach, on the other hand, requires no limiting process or subtraction of near-equal numbers. The results from Table 19 indicate that using the flux-based approach with 10^3 samples is superior to the finite difference method with 10^6 samples.

Table 19 Coefficient of Variation (100 Trials) of Sensitivities with respect to Bounds as a Function of the Number of Samples

| | Flux-based | | Finite Difference | |
|-----------|---|---|---|---|
| # Samples | $\frac{\partial \mathcal{P}_f}{\partial a}$ | $\frac{\partial \mathcal{P}_f}{\partial b}$ | $\frac{\partial \mathcal{P}_f}{\partial a}$ | $\frac{\partial \mathcal{P}_f}{\partial b}$ |
| 10^3 | .076 | .063 | 4.4 | 8.9 |
| 10^4 | .019 | .022 | 2.1 | 1.8 |
| 10^5 | .0076 | .0076 | .61 | 0.66 |
| 10^6 | .0021 | .0025 | .16 | 0.22 |

4. Conclusions

Development of probabilistic sensitivities is frequently considered an essential component of a probabilistic analysis and often critical towards understanding the physical mechanisms underlying failure and modifying the design to mitigate and manage risk. As a result, it is useful to explore and enhance the probabilistic sensitivity methods that are available for analysis. In this work, three sensitivity approaches were developed and applied. In particular, the developments accomplished include: 1) a new method to compute the sensitivity of the probability-of-failure with respect to the parameters that define the probability of detection curve of an NDE, 2) the investigation of complex variable methods for sensitivity analysis of structures using finite element analysis, and 3) enhancements to the score function method to compute the sensitivity with respect to bounds of truncated distributions.

4.1 Conclusions

A probabilistic methodology was developed and verified to compute the sensitivity of the probability-of-failure with respect to parameters of a POD curve used during an inspection process. The methodology has several attractive features. The formulation is such that the probabilistic sensitivities can be obtained at negligible cost using standard (Monte Carlo) or other sampling (Latin hypercube, importance sampling) methods. The key is that the same samples used to compute probability-of-failure are reused to compute the sensitivities. As such, the methodology can be implemented in a post-processing non-intrusive manner thereby facilitating implementation with existing or commercial codes; the methodology only needs the crack sizes at the times of inspection and the cycles-to-failure for each realization.

The formulation is generic and not limited to any specific random variables, fracture mechanics formulation, or any specific POD curve as long as the POD is modeled parametrically. The example problems demonstrated sensitivities with respect to two parameters of the lognormal-form POD curve but any POD form with any number of parameters can be used if the Ω term can be calculated.

The resulting equations are remarkably simple and involve an evaluation and summation of an Ω term with the summation occurring only for samples that have failed before time t and the evaluation occurs only at the time of inspection. The form of Ω requires the derivative of the POD curve with respect to its parameters and can be derived analytically. The time dependent nature of the sensitivity is accounted for by the time dependent indicator function term. The sensitivity equations for a particular inspection are unchanged in form due to subsequent inspections however their numerical evaluation may change due to samples being detected and removed by subsequent inspections.

4.2 Conclusions

Complex Taylor series expansion (CTSE), Fourier differentiation (FD), and central differencing (CD) can all be used to calculate shape sensitivities. To our knowledge, the work presented here marks the first time that FD has been used for calculating finite element shape sensitivities.

Experience shows that each method can compute reasonably accurate first order derivatives; however, the complex variable methods are attractive in that they are extremely robust to the complex step size h whereas finite difference is not. For 2-D finite element problems using second order shape functions, the error in the model was greater than the error due to the truncation errors associated with the numerical differentiation methods. This means that the complex variable sensitivity methods do not offer extra accuracy compared to CD if the model is not sufficiently accurate. They do, however, offer some ease in implementation. If the model were made to be more accurate, such as with higher order basis functions or more elements, then FD and CTSE could offer improved accuracy with respect to CD.

It has been shown that FD is capable of producing highly accurate sensitivities for functions with solutions that are accurate to machine precision [27]. The trade-off for the increased accuracy of FD is the requirement of several complex sample points. It may take as much as three times more computational effort to generate a complex sample than a real valued sample. Thus for the problems described in this paper, FD is not a good choice for shape sensitivity calculations, due to the limited accuracy of the solution. CTSE requires only half of the number of sample points required by CD, thus CTSE only requires about 1.5 times more computational effort than CD, at most. When the evaluation of a shape sensitivity requires displacement of only a small proportion of nodal ordinates the additional computational effort may be much less. This coupled with the fact that CTSE doesn't require changing the location of nodes in the complex plane means that it may still be a good choice for shape sensitivity problems.

One of the biggest problems with CD is that it requires the user to change the location of multiple nodes and maybe surrounding elements to implement a change in the desired shape. This may lead to elements with poor aspect ratios, or require complete remeshing of the domain, or both. This is especially true when the step size is rather large. Since CTSE does not require moving the nodes in the real plane, remeshing is not required, and there is less concern over the aspect ratio of the elements. Furthermore, if only the first order sensitivity is required, then the step size can be made very small without fear of increasing the round-off error.

4.3 Conclusions

Efficient evaluation of the sensitivity of the probability-of-failure or the response moments to the bounds of truncated distributions can provide useful information in the design stage in order to optimize product reliability, minimize cost, determine quality assurance procedures, etc. The method outlined here can be used to compute these sensitivities with a significant improvement in computational efficiency over standard finite difference methods.

The methodology is based upon an application of the material derivative concept to the probability-of-failure or the response moment integrals thus yielding a flux integral that must be computed in addition to the standard probability-of-failure or response integrals. The methodology is applicable to any limit state formulation, either component or system, and any random variables described by a truncated joint probability density function containing either correlated, e.g., truncated multivariate normal, or independent random variables.

The sensitivities require a supplemental flux integral for each bound that, when combined with the probability-of-failure and kernel functions, provides the sensitivity with respect to the bound

of a truncated distribution. However, the flux integral itself is a probability integral and, therefore, amenable to solution using existing probabilistic methods. If sampling is used to compute the probability-of-failure, the samples can be reused to compute flux integrals by projecting the samples to the bound of interest. Thus, the flux integrals are computed with negligible additional computation.

The superiority of the flux-based approach over the standard finite difference method was clearly evident from numerical studies using Monte Carlo sampling that indicated that the estimate of the sensitivities using the flux-integral approach required approximately 4 orders of magnitude fewer samples for the same accuracy as a standard finite difference approach.

5. Recommendations

The field of probabilistic sensitivity analysis is a critical aspect of probabilistic analysis. In order to put the results of a probabilistic analysis into practice, it is necessary to know the relative importance of the variables to the problem at hand. This is very dynamic and evolving field with the work describing only portion of the methods in the literature. In effect, the field largely did not exist 20 years ago. Hence it is incumbent upon the analyst to stay abreast of the latest developments.

Although significant progress has been made, there are still challenges to be overcome. The tension of computational efficiency versus accuracy is a continual challenge. For example, the Score Function method provides sensitivities for negligible cost since the Monte Carlo samples are reused, however, the variance of the sensitivities may be too large. As a result, accurate quantification of the sensitivities may require significantly more samples than used to compute the probability-of-failure or the response moments. This is likely to be true for variables of secondary importance but maybe true for primary variables also. Thus, new methods that provide accurate sensitivity information for minimal cost are still needed.

The complex variable sensitivity methods investigated provide an exciting new approach to calculate sensitivities of all types. This is especially true for shape sensitivities as the only the affected nodes need to be perturbed along the imaginary axis – no modifications to the real mesh are required. Since the mathematics are general, it is incumbent that we explore further applications and derivations of this method.

6. References

1. Grandt AF Jr., Fundamentals of Structural Integrity, Damage tolerant design and nondestructive evaluation, J. Wiley & Sons, Inc., 2004.
2. Harris DO, Dedhia, DD, Lu SC, Theoretical and user's manual for pc-PRAISE, Report no. NUREG/CR-5864, Nuclear Regulatory Commission, Washington, DC, 1992.
3. Simonen FA, Khaleel MA, Effects of Flaw Sizing Errors on the Reliability of Vessels and Piping J. Pressure Vessel Technol. 1998; V 120, 4, 365-73 doi:10.1115/1.2842345.
4. Pugh CE, Bass BR, Dickson TL, Role of probabilistic analysis in integrity assessments of reactor pressure vessels exposed to pressurized thermal-shock conditions, Engineering Failure Analysis, 2007; Vol. 14, No. 3, 501-517.
5. Carvalho AA, Rebello JMA, Souza MPV, Sagrilo LVS, Soares SD, Reliability of non-destructive test techniques in the inspection of pipelines used in the oil industry, International Journal of Pressure Vessels and Piping, Vol. 85, No. 11, 2008; 745-751.
6. Berens A, Probability of Detection (POD) Analysis for the Advanced Retirement for Cause (RFC)/Engine Structural Integrity Program (ENSIP) Nondestructive Evaluation (NDE) System Development, Volume 1 – POD Analysis, AFRL-ML-WP-TR-2001-4010, Jan. 2000.
7. Miedlar P, Berens A, Hovey P, Boehnlein T, Loomis J, "PRoF v3 PRobability Of Fracture," University of Dayton Research Institute, USAF Contract Number F09650-03-D-0001, December 2005.
8. Nondestructive Evaluation System Reliability Assessment, MIL-HDBK-1823, 30 April 1999.
9. Leverant GR, Millwater HR, McClung RC, Enright MP, A New Tool for Design and Certification of Aircraft Turbine Rotors, Journal of Engineering for Gas Turbines and Power, 2004; Vol. 126, No. 1, 155-159.
10. Wu Y-T, Enright MP, Millwater HR, Probabilistic Methods for Design Assessment of Reliability with Inspection, AIAA Journal, 2002; V40, No. 5, 937-946.
11. Rouhan, A, Schoefs, F, Probabilistic Modeling of Inspection Results for Offshore Structures, Structural Safety, 2003; Vol. 25, 379-399.
12. Rummel W, Hardy GL, TD Cooper, Applications of NDE Reliability to Systems, ASM Handbook, Vol. 17: Nondestructive Evaluation and Quality Control, ASM International, Materials Park, OH, 1989.
13. J. Garza, H. Millwater, "Sensitivity of Probability-of-Failure Estimates with respect to Probability of Detection Curve Parameters," submitted to Int. J. Pressure Vessels and Piping, June 2010.
14. Lyness, J.N., Moler, C.B., "Numerical Differentiation of Analytic Functions," *SIAM Journal of Numerical Analysis*, Vol. 4, No. 2, 1967, pp. 202-210.
15. Lyness, J.N., "Differentiation Formulas for Analytic Functions," *Mathematics of Computation*, Vol. 22, No. 102, 1968, pp. 352-362.
16. Squire, W., Trapp, G., "Using Complex Variables to Estimate Derivatives of Real Functions," *SIAM Review*, Vol. 40, No. 1, 1998, pp. 110-112.
17. Anderson, W.K., Newman, J.C., Whitfield, D.L., Nielsen, E.J., "Sensitivity Analysis for Navier-Stokes Equations on Unstructured Meshes Using Complex Variables," *AIAA Journal*, Vol. 39, No. 1, 2001, pp. 56-63.

18. Newman, J.C., Whitfield, D.L., Anderson, W.K., "Step-Size Independent Approach for Multidisciplinary Sensitivity Analysis," *Journal of Aircraft*, Vol. 40, No. 3, 2003, pp. 566-573.
19. Burg, C.O.E., Newman, J.C., "Computationally Efficient, Numerically Exact Design Space Derivatives via the Complex Taylor's Series Expansion Method," *Computers and Fluids*, Vol. 32, No. 3, 2003, pp. 373-383.
20. Cervino, L.I., Bewley, T.R., "On the Extension of the Complex-Step Derivative Technique to Pseudospectral Algorithms," *Journal of Computational Physics*, Vol. 187, No. 2, 2003, pp. 544-549.
21. Gao, X.W., He, M.C., "A New Inverse Analysis for Multi-Region Heat Conduction BEM Using Complex-Variable-Differentiation Method," *Engineering Analysis with Boundary Elements*, Vol. 29, No. 8, 2005, pp. 788-795.
22. Kim, J. Bates, D.G., Postlethwaite I., "Nonlinear Robust Performance Analysis Using Complex-Step Gradient Approximation," *Automatica*, Vol. 42, No. 1, 2006, pp. 177-182.
23. Wang, B.P., Apte, AP, "Complex Variable Method for Eigensolution Sensitivity Analysis," *AIAA Journal*, Vol. 44, No. 12, 2006, pp. 2958-2961.
24. Butuk, N., Pemba, J.P., "Computing CHEMKIN Sensitivities Using Complex Variables," *Transactions of the ASME*, Vol. 125 No. 3, 2003, pp. 854-858.
25. Lyness, J.N., Sande, G., "ENTCAF and ENTCRE: Evaluation of Normalized Taylor Coefficients of an Analytic Function," *Communications of the ACM*, Vol. 14, No. 10, 1971, pp. 669-675.
26. Henrici, P., "Fast Fourier Methods in Computational Complex Analysis," *SIAM Review*, Vol. 4, No. 11, 1979, pp. 481-527.
27. Bagley, R.L., "On Fourier Differentiation – A Numerical Tool for Implicit Functions," *International Journal of Applied Mathematics*, Vol. 19, No. 3, 2006, pp. 255-281.
28. Voorhees, A., "Complex Variable Sensitivity Methods for Finite Element Analysis", MS Thesis, University of Texas at San Antonio, May 2009, pp. 17.
29. Sadd, M.H., *Elasticity: Theory and Applications and Numerics*, Elsevier, New York, 1st Ed., 2005.
30. T.L. Anderson, *Fracture Mechanics, Fundamentals and Applications*, 3rd Ed., 2004.
31. *The Stress Analysis of Cracks Handbook*, 2nd E., Tada, Paris, and Irwin, 1985.
32. *Handbook of Physical Testing of Paper, Volume 1*, Richard E. Mark, Jens Borch, Charles Habeger, eq. (28), pg. 463.
33. R. J. Sanford, *Principles of Fracture Mechanics*, eq. (3.57), 2003, Pearson Education, Inc.
34. Rubinstein RY and Shapiro A, *Discrete Event Systems, Sensitivity Analysis and Stochastic Optimization by the Score Function Method*. J. Wiley & Sons, Chichester, England, 1993.
35. H.R. Millwater, and Y. Feng, "Probabilistic Sensitivity Analysis with respect to Bounds of Truncated Distributions," *ASME J. Mech. Design*, (accepted).
36. Fung YC, *Foundations of Solid Mechanics*, Prentice-Hall, (1965) pp. 120-121

LIST OF ACRONYMS, ABBREVIATIONS, AND SYMBOLS

| ACRONYM | DESCRIPTION |
|----------|--|
| POD | Probability-of-Detection |
| P_f | Probability-of-failure |
| f_X | Joint density function |
| I | Indicator function |
| X | Vector of random variables |
| a | Crack size |
| t | Time or cycles-to-failure |
| θ | Parameter of POD curve |
| Ω | Kernel function for POD sensitivity analysis |
| C | Paris crack growth constant |
| m | Paris crack growth exponent |
| a_c | Critical crack size |
| g | Limit state |
| K_{IC} | Fracture toughness |
| K | Stress intensity factor |
| K' | Derivative of K with respect to crack length |